Available online at www.sciencedirect.com

ScienceDirect

Geochimica et Cosmochimica Acta 250 (2019) 49–75

Geochimica et Cosmochimica Acta

www.elsevier.com/locate/gca

Secular mantle oxidation across the Archean-Proterozoic boundary: Evidence from V partitioning in komatiites and picrites

Robert W. Nicklas [a,*], Igor S. Puchtel [a], Richard D. Ash [a], Philip M. Piccoli [a], Eero Hanski [b], Euan G. Nisbet [c], Pedro Waterton [d], D. Graham Pearson [d], Ariel D. Anbar [e]

[a] Department of Geology, University of Maryland, College Park, MD 20742, USA
[b] Oulu Mining School, University of Oulu, P.O. Box 3000, FI-90014, Finland
[c] Dept. Earth Sciences, Royal Holloway, Univ. of London, Egham TW20 0EX, United Kingdom
[d] Earth and Atmospheric Sciences Department, University of Alberta, Edmonton, Alberta T6G 2E3, Canada
[e] School of Earth and Space Exploration, Arizona State University, Tempe, AZ 85287, USA

Received 16 July 2018; accepted in revised form 23 January 2019; available online 1 February 2019

Abstract

The oxygen fugacities of nine mantle-derived komatiitic and picritic systems ranging in age from 3.55 Ga to modern day were determined using the redox-sensitive partitioning of V between liquidus olivine and komatiitic/picritic melt. The combined set of the oxygen fugacity data for seven systems from this study and the six komatiite systems studied by Nicklas et al. (2018), all of which likely represent large regions of the mantle, defines a well-constrained trend indicating an increase in oxygen fugacity of the lavas of ~1.3 ΔFMQ log units from 3.48 to 1.87 Ga, and a nearly constant oxygen fugacity from 1.87 Ga to the present. The oxygen fugacity data for the 3.55 Ga Schapenburg komatiite system, the mantle source region of which was previously argued to have been isolated from mantle convection within the first 30 Ma of the Solar System history, plot well above the trend and were not included in the regression. These komatiite's anomalously high oxygen fugacity data likely reflect preservation of early-formed magma ocean redox heterogeneities until at least the Paleoarchean.

The observed increase in the oxygen fugacity of the studied komatiite and picrite systems of ~1.3 ΔFMQ log units is shown to be a feature of their mantle source regions and is interpreted to indicate secular oxidation of the mantle between 3.48 and 1.87 Ga. Three mechanisms are considered to account for the observed change in the redox state of the mantle: (1) recycling of altered oceanic crust, (2) venting of oxygen from the core due to inner core crystallization, and (3) convection-driven homogenization of an initially redox-heterogeneous primordial mantle. It is demonstrated that none of the three mechanisms alone can fully explain the observed trend, although mechanism (3) is best supported by the available geochemical data. These new data provide further evidence for mantle involvement in the dramatic increase in the oxygen concentration of the atmosphere leading up to the Great Oxidation Event at ~2.4 Ga.

Keyword: Mantle redox

* Corresponding author.
E-mail address: rnicklas@umd.edu (R.W. Nicklas).

https://doi.org/10.1016/j.gca.2019.01.037
0016-7037/

1. INTRODUCTION

The oxidation state of the mantle is an important intensive thermodynamic parameter that controls the geochemical behavior of redox-sensitive elements in igneous systems (Herd, 2008), and that may be intimately linked to the oxidation state of the atmosphere (Holland, 2002).

Due to its large variation in natural systems, and to minimize the relative effects of temperature and pressure, the oxidation state of the mantle is quantified in terms of log units ($\Delta\log fO_2$) relative to various mineral assemblage buffers, such as the nickel-nickel oxide (NNO) and the fayalite-magnetite-quartz (FMQ) buffers. There are several methods that are currently used to determine fO_2 of igneous rocks and their mantle sources, including using experimentally calibrated equilibria (Sack et al., 1980; Ballhaus et al., 1991) in pristine mantle- and mantle-derived igneous rocks, utilizing measurements of $Fe^{3+}/\Sigma Fe$ in spinels (Canil et al., 1994) or fresh volcanic glasses, respectively (Cottrell et al., 2009). For most samples in the geological record, however, this approach cannot be used, as the $Fe^{2+}/\Sigma Fe$ ratio of minerals and glasses can be readily reset during alteration and metamorphism, although volcanic glass can be preserved as olivine-hosted melt inclusions in rocks as old as 2.69 Ga (e.g., Berry et al., 2008). Additionally, the $Fe^{3+}/\Sigma Fe$ of volcanic glasses can be affected by syn-eruptive processes, such as sulfur degassing (Moussallam et al., 2014, 2016).

Because of the inapplicability of the $Fe^{2+}/\Sigma Fe$ oxybarometer to altered samples, alternative methodology has been used, including determination of the stable Fe isotopic composition in rocks and minerals (Williams et al., 2005, 2009; Dauphas, 2009), quantification of ratios of redox-sensitive to redox-insensitive elements (Li and Lee, 2004; Aulbach and Viljoen, 2015; Aulbach and Stagno, 2016), or modeling partitioning behavior of redox-sensitive elements, such as V or Cr, during magmatic differentiation (Canil, 1997; Canil and Fedortchouk, 2001; Delano, 2001; Mallmann and O'Neill, 2009, 2013; Nicklas et al., 2016, 2018).

Most studies have concluded that mantle fO_2 has remained constant since at least the early Archean (Canil, 1997; Canil and Fedortchouk, 2001; Delano, 2001; Li and Lee, 2004; Berry et al., 2008; Trail et al., 2011; Hibbert et al., 2012). Recently, however, some researchers have argued for an increase in fO_2 of the upper mantle since the early Archean by as much as ~0.9 log units (e.g., Aulbach and Viljoen, 2015; Aulbach and Stagno, 2016; Shu et al., 2016; Aulbach et al., 2017a), while others have reported data that suggest the possibility of an increase in fO_2 of the mantle during the Archean (Nicklas et al., 2018). Because even small changes in mantle redox conditions can have large effects on the chemical evolution of major terrestrial reservoirs, such as the atmosphere, further constraints on mantle redox evolution are necessary.

Nicklas et al. (2016, 2018) determined the fO_2 of six Archean komatiite systems ranging in age from 3.48 to 2.41 Ga and showed that their entire range of oxygen fugacities was within the uncertainties of that for modern MORB at the 2-sigma uncertainty level. However, the data defined a distinct trend indicative of an increase in mantle fO_2 with time at the 1-sigma uncertainty level. In this study, we determined the fO_2 of nine additional komatiite and picrite systems. With the exception of the 3.55 Ga Schapenburg komatiite system, all the new systems are post-Archean in age.

Our use of ultramafic lavas to ascertain mantle fO_2 deserves justification because the vast majority of mantle-derived post-Archean volcanism is basaltic in nature. We argue that komatiites and picrites provide unique insights into mantle fO_2 for several reasons. First, it has been shown that island arc basalts can be up to ~6.0 log fO_2 units more oxidized than MORB or OIB (Carmichael, 1991) and this high fO_2 is likely a result of subduction-related metasomatism in their mantle wedge source region (Kelley and Cottrell, 2012; Brounce et al., 2014). We, therefore, avoided the potential complicating factor of including subduction-related lavas and, instead, opted for rocks that have been argued to be derived from anhydrous melting in hot mantle upwellings, or plumes. Second, work on two separate modern OIB systems demonstrated a strong correlation between measured $Fe^{3+}/\Sigma Fe$ and sulfur content of volcanic glasses, with degassing of SO_2 having a reducing effect on the melt (Kelley and Cottrell, 2012; Moussallam et al., 2014, 2016). Based on the results of previous studies that demonstrated incompatible behavior of Pd and Pt in sulfur-undersaturated systems (i.e. Brügmann et al., 1987; Puchtel et al., 2016a), the level of saturation of sulfur species, if any, can be detected and corrected for in all the systems studied. In contrast, MORB lavas have been shown to be, to various degrees, sulfide- and vapor-saturated upon emplacement (e.g., Mathez, 1976; Bottinga and Javoy, 1990; Le Voyer et al., 2015), and their oxygen fugacities were likely affected by sulfur degassing. The komatiite and picrite systems we selected for this study were mostly produced by large degrees of partial melting of the mantle and, therefore, the compositions of the studied lavas are chemically similar to those of their mantle sources. Although the mantle source regions sampled by spreading ridges are not necessarily directly analogous to the mantle source regions tapped by anomalously hot plumes, comparing oxidation states of plume lavas serves as a valid proxy for the evolving oxidation state of the mantle. Even if there are differences in redox state between plume source mantle and ridge source mantle, there is no *a priori* reason why the relative difference between those two sources should change with time. This allows for the comparison of plume lavas to one another in order to constrain the redox evolution of the bulk mantle.

The method we applied in this study relies on the redox-sensitive nature of V partitioning between liquidus olivine and komatiitic and picritic magmas. The method was developed by Nicklas et al. (2016, 2018) and utilizes experimental data from Canil (1997) and Canil and Fedortchouk (2001). It was previously applied to six Archean komatiite systems by Nicklas et al. (2016, 2018), and the results of those studies will be considered in concert with the new results in order to constrain the redox evolution of the mantle since the early Archean.

2. GEOLOGICAL BACKGROUND OF RESEARCH TARGETS

In this study, whole-rock samples and near-liquidus olivine from nine komatiite and picrite systems have been analyzed for trace metal abundances. These include the 3.55 Ga Schapenburg komatiites from the Barberton Greenstone Belt (BGB) in the Kaapvaal Craton, South Africa, the 2.06 Ga Lapland komatiites and the 1.98 Ga Onega Plateau picrites in the Fennoscandian Shield, the 1.87 Ga Winnipegosis komatiites of the Superior Craton, Canada, the 0.251 Ga Song Da komatiites, Vietnam, the 0.089 Ga komatiites of Gorgona Island, Colombia, the 0.062 Ga picrites of Padloping Island, Canada, and modern picrites from the Kilauea Iki lava lake in Hawaii and the Western Rift Zone of Iceland.

2.1. The 3.55 Ga Schapenburg komatiite system, Barberton Greenstone Belt, South Africa

The Schapenburg Greenstone Remnant (SGR) is a 12×2.5 km sequence of alternating volcanic and marine sedimentary rocks in the Kaapvaal Craton, South Africa (Anhaeusser and Robb, 1980). The sequence is correlated with the lowermost formations of the Onverwacht Group of the Barberton BGB (Viljoen and Viljoen, 1969). The Onverwacht Group contains, among others, the 3.48 Ga Komati and 3.26 Ga Weltevreden Formations, which were previously studied for their fO_2 by Nicklas et al. (2018). The volcano-sedimentary sequence of the SGR is cyclic in nature, consisting of komatiites, komatiitic basalts, and banded iron formations (Anhaeusser and Robb, 1980).

The SGR komatiites are typical Al-depleted komatiites ($Al_2O_3/TiO_2 = 10.0 \pm 0.8$, $Gd/Yb_N = 1.57 \pm 0.03$) and are also slightly depleted in LREE ($La/Sm_N = 0.93 \pm 0.04$). Using the Re-Os system, the SGR samples have been directly dated at 3550 ± 87 Ma (Puchtel et al., 2016a). The petrology and geochemistry of the Schapenburg komatiites have been studied using both outcrop samples (Lecuyer et al., 1994; Blichert-Toft et al., 2004; Puchtel et al., 2009) and in drill core samples (Puchtel et al., 2016a). The sample powders analyzed in this study are those prepared by Puchtel et al. (2016a); all samples came from a single differentiated komatiite lava flow.

The SGR komatiites are of particular interest as they display negative ^{182}W and ^{142}Nd anomalies ($\mu^{182}W = -8.4 \pm 4.5$, $\mu^{142}Nd = -4.9 \pm 2.8$), due to their derivation from an early-formed (within the first 30 Ma of the Solar System history) mantle source that experienced fractionation of lower mantle phases, such as Ca-perovskite and bridgmanite (Puchtel et al., 2016a). The long-lived ^{147}Sm-^{143}Nd and ^{176}Lu-^{176}Hf systems (initial $\varepsilon^{143}Nd = +2.4 \pm 0.1$, initial $\varepsilon^{176}Hf = +5.7 \pm 0.3$) are decoupled, plotting off the terrestrial mantle array at 3.55 Ga, also likely due to early lower-mantle magma ocean processes (Puchtel et al., 2016a). The SGR mantle source has been calculated to contain $29 \pm 5\%$ of the total HSE abundances estimated for the modern BSE, indicating that the SGR source region did not receive the full complement of chondritic late accretion component (Puchtel et al., 2016a). Finally, the initial $\gamma^{187}Os$ value of $+3.7 \pm 0.2$ indicates derivation from a source with a long-term supra-chondritic Re/Os established early in Earth's history. Additional information on the SGR komatiites can be found in Anhaeusser (1983, 1991), Anhaeusser and Robb (1980), Lecuyer et al. (1994), Blichert-Toft et al. (2004), and Puchtel et al. (2009, 2016a).

2.2. The 2.06 Ga Lapland komatiite system, Fennoscandian Shield

The geology of Finnish Lapland is dominated by the Paleoproterozoic Central Lapland Greenstone Belt (CLGB), consisting of a thick succession of metamorphosed supracrustal rocks ranging in age from ca. 2.5 to 1.9 Ga (Hanski and Huhma, 2005). The Savukoski Group, in the upper section of the CLGB, consists of fine-grained sedimentary rocks overlain by Ti-rich komatiites and picrites, which have been associated with mantle plume activity (Hanski et al., 2001). The komatiites of this group have been directly dated at 2056 ± 25 Ma using the Sm-Nd method on primary clinopyroxenes (Hanski et al., 2001). This age is consistent with the U-Pb zircon age of 2058 ± 4 Ma obtained for the Kevitsa mafic-ultramafic intrusion cutting phyllites of the Savukoski Group (Mutanen and Huhma, 2001). The Kevitsa intrusion is cut by ultramafic dikes, termed "Kevitsa dikes", which have very similar chemical and isotopic compositions to those of komatiitic lavas of the Savukoski Group, including unique hump-shaped chondrite-normalized REE patterns (Hanski et al., 2001), and it was argued, based on several lines of evidence, that the dikes served as feeding magma conduits to the komatiites (Huhma et al., 2018). The CLGB komatiites have yet to show preservation of igneous olivine, and were, thus, unsuitable for this study. However, unlike the CLGB komatiites, the Kevitsa dikes display excellent preservation of igneous minerals (Fig. 1a). The studied dike is ~5 m in thickness and is characterized by internal differentiation related to fractionation of olivine, with a coarse-grained olivine-enriched central part and finer-grained chilled zones near contacts with the host rocks. The chilled margins of the dike consist of glassy, olivine phenocryst-poor komatiite. Additional information on the CLGB komatiites and Kevitsa dikes can be found in Hanski et al. (2001) and Huhma et al. (2018).

2.3. The 1.98 Ga Onega Plateau picrite system, Fennoscandian Shield

The Onega Plateau is a large (~35,000 km^2) continental flood basalt province within the central Karelian Province of the Fennoscandian Shield (Puchtel et al., 1998a). The flood basalts are divided into two sequences, the lower Jatulian sequence, ~700 m in thickness, and the upper Ludikovian sequence, which is further subdivided into the lower ~1800-m-thick Zaonega suite and the upper ~700-m-thick Suisaarian suite (Puchtel et al., 1998a). It has been proposed by those authors that the Onega Plateau was emplaced rapidly onto submerged continental crust in a single starting mantle plume environment, with the plume

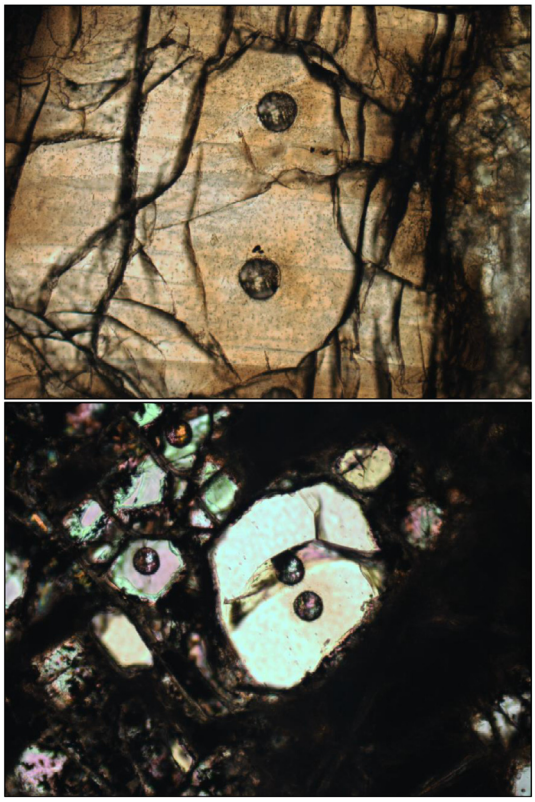

Fig. 1. (A) Photomicrograph of thin section sample KD08 from the Lapland komatiite system. A large olivine phenocryst is shown with two 100 μm LA-ICP-MS pits in its core. (B) Photomicrograph of thin section sample RP1A-8 from the Winnipegosis komatiite system. Olivine phenocrysts are shown with 80 μm LA-ICP-MS pits. Both images were taken with cross-polarized light using 120 μm thick slides, and have a field of view of 3.0 × 2.5 mm.

head being ~2000 km in diameter. The samples chosen for this study come from the Konchozero sill, which served as a feeding magma conduit to the Suisaarian suite picrites. The sill ranges in thickness from a few tens of meters at its periphery to over 200 m in its central zone. The sill has a 4- to 6-m-thick glassy chilled margin close to its contact with the country rocks, and displays significant variation in the abundance of olivine within the sill, demonstrating internal differentiation after emplacement (Puchtel et al., 1998b). Both the Konchozero sill and the Suisaarian suite picrites have elevated $(Nb/Th)_N$ of 1.4–2.4 and $(Nb/La)_N$ of 1.1–1.3, and a positive initial ε_{Nd} value of $+3.2 \pm 0.1$, indicating that they did not experience any significant crustal contamination (Puchtel et al., 1998a). The Konchozero sill has been dated at 1969 ± 18 Ma by the Re-Os isochron method on whole-rock samples and primary minerals, which is consistent with the Sm-Nd and Pb-Pb isochron ages of 1988 ± 34 Ma and 1985 ± 57 Ma, respectively, determined for the same samples (Puchtel et al., 1998b). Although the Suisaarian suite picrites do not preserve igneous olivine due to seafloor alteration and prehnite-pumpellyite facies metamorphism, a number of Ol-Cpx cumulate samples from the Konchozero sill that show good preservation of olivine have recently been identified. These samples were the ones selected for our study, and new sample powders and thin sections were prepared. Additional information on both the Onega Plateau picrites and the Konchozero sill rocks can be found in Puchtel et al. (1998a,b).

2.4. The 1.87 Ga Winnipegosis komatiite system, Canadian Shield

The Winnipegosis Komatiite Belt (WKB) is located on the western edge of the Archean Superior Craton, Manitoba, Canada, and is spatially associated with the Thompson Nickel Belt, with both belts comprising parts of the larger Paleoproterozoic Circum-Superior Belt (Hulbert et al., 1994). The latter belt consists of a 3000-km-long band of bimodal felsic-mafic volcanism along the western and northern edges of the Superior Craton (Baragar and Scoates, 1981), and has been interpreted as a tectonically emplaced large igneous province (LIP) (Ernst and Bleeker, 2010). The ~150 × 30-km-sized WKB is covered by a 120-to-500-m-thick sequence of Paleozoic sedimentary rocks and is dominated by komatiitic basalts and komatiites, with minor carbonate and shale sediments (McGregor, 2011). Due to the lack of surface exposure of the WKB, all samples of the belt were collected from drill core. The komatiites are remarkably well preserved, having only experienced sub-greenschist facies metamorphism and minimal aqueous alteration (Waterton et al., 2017) and retain large equant olivine phenocrysts (Fig. 1b). The komatiites belong to the Al-undepleted type ($Al_2O_3/TiO_2 = 17.2 \pm 1.1$, $Gd/Yb_N = 1.13 \pm 0.04$) and are dominated by massive olivine-porphyritic flows (Waterton et al., 2017). U-Pb zircon dating of basaltic flows within the WKB yielded a weighted average $^{207}Pb/^{206}Pb$ age of 1870 ± 7 Ma (Waterton et al., 2017). For this study, we used samples representing several massive Ol-porphyritic komatiite lava flows. Additional information on the WKB komatiites can be found in Hulbert et al. (1994), McGregor (2011), and Waterton et al. (2017).

2.5. The 251 Ma Song Da komatiite system, Vietnam

The Song Da Zone (SDZ) is a Permian supracrustal belt ~20 × 250 km in size in northwestern Vietnam running parallel to the Red River Fault (Polyakov et al., 1991; Hanski et al., 2004). The SDZ is closely associated with the Emeishan LIP in SW China, and likely formed in the SW part of the Emeishan LIP before being displaced ~600 km southeast by the Red River Fault (Chung et al., 1997, 1998). The Emeishan LIP has been Ar-Ar dated at 251.2–252.8 Ma (Lo et al., 2002). The SDZ consists of carbonate and siliciclastic sediments surrounding a central band of mafic-ultramafic volcanic rocks (Polyakov et al., 1991). Flows of MgO-rich lavas within this central band have been termed either komatiites (Hanski et al., 2004) or picrites (Wang et al., 2007; Anh et al., 2011). In this study, following Hanski et al. (2004), we refer to them as komatiites, consistent with the presence of clinopyroxene spinifex textures in these lavas. Komatiites in the SDZ experienced greenschist facies metamorphism and relatively

minor aqueous alteration, with ~75% of their olivine phenocrysts preserved (Hanski et al., 2004). A Re-Os isochron obtained on whole-rock komatiite samples yielded an age of 270 ± 21 Ma and a chondritic initial γ^{187}Os value of +0.02 ± 0.40 (Hanski et al., 2004). The initial ε^{143}Nd values of the komatiites range from +3 to +8 reflecting varying, but small (2–3%), degrees of contamination with Proterozoic silicic basement material, as indicated by their moderate depletion in the highly incompatible lithophile trace elements ($La/Sm_N = 0.58 \pm 0.34$). The Song Da komatiites are typical Al-undepleted komatiites, with $Al_2O_3/TiO_2 = 20 \pm 5$ and $Gd/Yb_N = 0.97 \pm 0.23$ (Hanski et al., 2004). Komatiite whole-rock samples from the Na Muoi River region were analyzed in this study. More information on komatiites from the SDZ can be found in Polyakov et al. (1991), Hanski et al. (2004), Wang et al. (2007), and Anh et al. (2011).

2.6. The 89 Ma Gorgona komatiite system, Colombia

Gorgona is a ~2 × 8 km island off the Pacific coast of Colombia (Echeverria, 1980). High-MgO lavas found on Gorgona were first recognized to be Phanerozoic equivalents of Archean komatiites by Gansser et al. (1979) and Echeverria (1980), making them one of the rare examples of true Phanerozoic komatiites, and the youngest komatiites yet discovered. They are transitional between the Al-undepleted and Al-depleted types of komatiites ($Al_2O_3/TiO_2 = 18.5 \pm 0.9$, $Gd/Yb_N = 1.24 \pm 0.04$) and have coupled radiogenic ε^{143}Nd and ε^{176}Hf systematics (Thompson et al., 2003) and, thus, plot on the terrestrial array for these two isotopic systems. They have initial ε^{186}Os and γ^{187}Os ranging from 0 to +0.7 and from 0 to +12, respectively (Walker et al., 1999; Brandon et al., 2003), implying a substantial long-term heterogeneity in Re/Os and Pt/Os in the source of these lavas. Lead isotope data have shown resolvable differences between komatiites exposed on the east coast of the island and those exposed on the west coast (Dupre and Echeverria, 1984). Isotopic and trace element data imply that at least three, and possibly four, separate end member compositions were present in the mantle source region of the Gorgona lavas to explain the large diversity of geochemical signatures found on the island (Kerr, 2005).

Ar-Ar dating of Gorgona basalts has yielded a weighted mean age of 88.9 ± 1.2 Ma (Sinton et al., 1998), while a Re-Os isochron on the Gorgona basalts yielded an age of 89.2 ± 5.2 Ma (Walker et al., 1999). Due to the significant Os and Pb isotopic heterogeneity recognized within Gorgona komatiites, we have selected two komatiite groups from Gorgona Island for analysis, one on the eastern and another on the western side, and have determined the oxygen fugacity of each of the two groups. We analyzed samples collected by Revillon et al. (2000) (western group) and Echeverria (1980) (eastern group). All the samples studied were obtained as rock slabs from the Smithsonian National Museum of Natural History. They are characterized by superb state of preservation of primary minerals, and presence of abundant olivine phenocrysts. Additional geochemical information on the Gorgona komatiites is available in Echeverria (1980), Dupre and Echeverria (1984), Kerr et al. (1996), Walker et al. (1999), Revillon et al. (2000, 2002), Serrano et al. (2011) and Kerr (2005).

2.7. The 62 Ma Padloping Island picrites

Padloping Island is a ~6 × 2 km island located off the coast of southeastern Baffin Island, Nunavut, Canada (Clarke and Upton, 1971). The picrite lavas located on Padloping Island are genetically closely associated with those on Disko Island off the west coast of Greenland, as well as those from the Faroe Islands and the British Tertiary Volcanic Province, indicating a common plume origin for these lavas, which likely formed during the first interaction of the present-day Iceland plume with the lithosphere (White and McKenzie, 1989; Robillard et al., 1992). The total thickness of the exposed lava sequence does not exceed 750 m (Francis, 1985), and the lowermost 350 m of the sequence consist of subaqueously erupted lavas (Robillard et al., 1992). The Padloping picrites have not experienced any significant alteration due to their very young age (Clarke and Upton, 1971). The lavas have not been directly dated, but their magnetic polarization belongs to Chron27n (Deutsch et al., 1971), making it possible to correlate them with the Anaanaa member in west Greenland dated at 61.7–62.0 Ma (Pedersen et al., 2002). Samples from Padloping Island have been found to be among the lavas having the highest ^{3}He/^{4}He ratios on Earth, indicating that they sampled a primordial, undegassed reservoir (Stuart et al., 2003; Starkey et al., 2009). The lavas also possess very primitive Pb isotope compositions (Jackson et al., 2010), although it has been suggested that this was the result of crustal contamination with Archean gneisses (Dale, 2016). It has been recently recognized that the Padloping Island lavas have a large positive μ^{182}W anomaly, providing further evidence that the picrites sampled a mantle domain that was isolated from the convecting mantle within the first ~50 Ma of Earth's history (Rizo et al., 2016). However, the ^{146}Sm-^{142}Nd isotope system shows no anomaly in the Padloping Island picrites, indicating a decoupling of these short-lived isotopic systems in the mantle source of the lavas (De Leeuw et al., 2017). The average initial $^{187}Os/^{188}Os = 0.1272 \pm 0.0007$ determined for the lavas is chondritic, which indicates that the picrites had a negligible amount of ancient recycled crust in their source region (Dale et al., 2009), as would be expected for lavas sampling a very primitive source. Although samples from Padloping Island have not previously been the subject of oxygen fugacity measurements, the correlated Anaanaa unit in west Greenland has been determined to have an fO_2 close to $\Delta FMQ = +0.28$, based on the oxidation state of Fe in volcanic glasses (Larsen and Pedersen, 2000). We analyzed sample powders and thin sections previously studied by Kent et al. (2004), Dale et al. (2009) and Jackson et al. (2010). These samples were taken from subaqueously erupted pillow-textured picritic lava flows exposed on the northeastern shore of Padloping Island, in the lowermost 350 m of the volcanic sequence. Additional information on the

Padloping Island picrites can be found in Clarke and Upton (1971), Francis (1985), Kent et al. (2004), Dale et al. (2009) and Starkey et al. (2009).

2.8. The 1959 Kilauea Iki lava lake, Hawaii

The Kilauea Iki lava lake erupted over a four-week interval in 1959 (Richter and Moore, 1966), and has subsequently cooled and internally differentiated as a closed system. It has been extensively utilized as an excellent natural laboratory for studying igneous differentiation; the lava lake was drilled and sampled by the USGS throughout the 1960s, as it cooled and crystallized. The lava lake is picritic in composition, with the emplaced parental magma containing ~15 wt.% MgO (Wright, 1973). The lavas are strongly LREE-enriched, with $La/Sm_N = 1.7 \pm 0.1$ and they show steeply sloping chondrite-normalized REE patterns, with $La/Yb_N = 5.6 \pm 0.5$ (Helz, 2012), a feature common to many ocean island basalts. We utilized a set of surface outcrop samples that we collected in 2015 from across the upper chilled margin of the lava lake. The oxygen fugacity of the lava lake, corrected for sulfur degassing, has been previously estimated to be $\sim\Delta NNO = 0$ (Moussallam et al., 2016), using the $Fe^{3+}/\Sigma Fe$ ratio of melt inclusions, and this estimate will be further used to inter-calibrate our fO_2 data with the fO_2 data determined using the $Fe^{3+}/\Sigma Fe$ method. Background geochemical data on the Kilauea-Iki lava lake can be found in Pitcher et al. (2009) and Helz (2012).

2.9. Western Rift Zone picrites, Iceland

Iceland represents an important modern-day example of mantle plume-induced magmatic activity. The majority of Icelandic igneous rocks, including picrites, show isotopic evidence for recycled oceanic crust in their mantle source region (Hemond et al., 1993). There is also a primordial, undegassed component in many Icelandic lavas, as evidenced by their elevated $^3He/^4He$ ratios relative to MORB (Kurz et al., 1985). We selected Icelandic picrites for our study as another modern analogue to compare with Archean plume lavas. This study utilized thin sections and sample powders from Maelifell and Dagmalafell volcanoes, two spatially associated volcanoes in the Western Rift Zone (WRZ) of SW Iceland previously studied by Brandon et al. (2007). These samples have been shown to have moderately elevated $^3He/^4He$ (11.5–17.2) relative to MORB, and slightly elevated initial $^{187}Os/^{188}Os$ ratios (0.13305–0.13335), indicating that both a primordial and a recycled component are present in their mantle source region (Brandon et al., 2007). More information on the Western Rift Zone samples used in this study can be found in Brandon et al. (2007).

3. ANALYTICAL TECHNIQUES

The protocols we used to determine the oxygen fugacity of the studied komatiite and picrite systems closely follow those used by Nicklas et al. (2016, 2018), and are briefly summarized in the sections below.

3.1. Sample selection, crushing procedure, and major and minor element abundances

In this study, we either used the sample powders already available from previous studies, or prepared new powders. In the case of the Onega Plateau picrites, the Lapland, Song Da and Gorgona komatiites, and the Kilauea Iki lava lake, new sample powders were prepared. The protocol for preparation of these samples followed that described by Puchtel et al. (2016b). Hand specimens, between 200 and 500 g in size, were cut into slabs, abraded on the cut surfaces using SiC sandpaper to remove saw marks, crushed in an alumina jaw crusher, and finely ground using an alumina shatterbox and alumina disk mill.

The major- and minor element analyses for the whole-rock samples were carried out at Franklin & Marshall College, Lancaster, Pennsylvania, USA on fused glass discs using a Phillips 2404 XRF spectrometer, following the procedure of Mertzman (2000). Typical precision of the analyses was ~2% relative (2SD) for major elements with concentrations >0.5% and ~5% relative for the rest of the major elements and for minor elements, as indicated by the analysis of the USGS Geologic Reference Materials BIR-1 and BCR-1 as unknowns (Puchtel et al., 2016b).

3.2. Analysis of trace element abundances in the whole-rock samples

The abundances of the trace metals in the whole-rock samples were determined using the standard addition solution inductively-coupled plasma mass-spectrometry technique (SA ICP-MS), and following the protocols detailed in Nicklas et al. (2016) and Nicklas et al. (2018). The sample solutions were analyzed on a *ThermoFinnigan Element2* sector field ICP-MS at the *Plasma Laboratory (PL)*, Department of Geology, University of Maryland in medium resolution (MR) mode. The external precision (i.e., 2SD) of the procedure was previously found to be 5% or better for all the elements of interest (Nicklas et al., 2016, 2018), and this value was used as the uncertainty on V concentrations for all error propagation calculations. For additional details on the development of the high-precision trace metal analysis in komatiites, the reader is referred to Nicklas et al. (2016, 2018).

3.3. Electron probe microanalysis of liquidus olivine

Major element analyses of olivines were performed on polished thin sections using the *JEOL JXA 8900 R* electron probe microanalyzer at the *Advanced Imaging and Microscopy Laboratory (AIMLab)*, University of Maryland. Special attention was paid to select and analyze only early-crystallized, equant grains. Operating conditions were 15 keV accelerating potential, 20 nA beam current, and 10 μm spot size. These electron probe data were then used

for data normalization purposes for the laser ablation analysis, and to calculate the emplaced lava composition of each system, as described in Section 3.4.

3.4. Determination of the composition of the emplaced komatiite lavas

All the whole-rock samples studied, except for the upper chilled margin samples, have likely fractionated olivine post-emplacement and, therefore, the MgO contents of these whole-rock samples do not reflect that of the emplaced lava from which the olivine phenocrysts formed, due to addition or subtraction of cumulate olivine. Calculation of the emplaced lava MgO content for each komatiite and picrite system allows us to estimate the abundances of incompatible elements, most importantly V, in the emplaced lavas. The approach we used to calculate the emplaced lava MgO content was developed by Arndt (1986a) and Barnes et al. (1988) and has been widely used in follow-up studies of komatiites. This approach is based on the well-established Fe-Mg relationship between the composition of olivine and that of the liquid from which it crystallized (Roeder and Emslie, 1970; Beattie et al., 1991). The highest MgO and lowest FeO contents of the cores of equant olivine grains, as determined via EPMA (see Section 3.3), and the compositions of the komatiite liquids in equilibrium with these olivine compositions, were estimated using the partition coefficient $D_{Mg\text{-}Fe}^{Ol\text{-}Liq} = 0.30$ from Beattie et al. (1991). The whole-rock FeO contents of chilled margin samples from each komatiite system were used as a proxy for emplaced lava FeO content. For additional details on this protocol, the reader is referred to the publications by Puchtel et al. (2004, 2009, 2013, 2016b) and Nicklas et al. (2016, 2018).

3.5. Laser ablation ICP-MS analysis of liquidus olivine

Olivine grains were studied in polished thin sections in all komatiite and picrite systems except for the Western Gorgona and Schapenburg komatiites, and Kilauea Iki and Padloping Island picrites, for which polished rock chips mounted in epoxy were used.

The olivine grains were analyzed using an *UP213 New Wave* laser-ablation system coupled to the *ThermoFinnigan Element2* ICP-MS at *the PL*. The quintupled Nd-YAG laser operated at 7 Hz with fluence controlled between 2 and 4 J/cm^2 (~60% laser power). The analyses were conducted in low resolution (LR) mode, as this has been found to provide adequate resolution for V analyses in olivine (Aulbach et al., 2017b). Before each analysis, the surface was ablated briefly to remove surface contamination, and the signal was allowed to drop to the baseline level before the analysis was begun. The spot size of each analysis varied between 55 and 100 μm depending on the size and homogeneity of the grains analyzed. Only equant olivine grains containing no visible inclusions were selected for analysis. Typically, the small size of the olivine grains permitted only one laser spot per each grain. Photomicrographs of the olivines from the Lapland komatiitic dike (a) and a massive komatiite sample from Winnipegosis (b) of the type that were selected for analysis are shown in Fig. 1. Replicate analyses of the USGS Microanalytical Reference Materials BHVO-2G and BCR-2G were performed with each set of 12–16 spots analyzed. The raw data were reduced using the *LAMTRACE* software and the lowest FeO abundances for the olivine in each komatiite and picrite system, determined by EPMA analysis, were used as normalizing values. The 2SD of the mean was used as a measure of the uncertainty on the calculated average concentrations of trace metals in olivine for the individual samples.

4. RESULTS

4.1. Trace metal abundances in the liquidus olivine

Average concentrations of V, Sc, Ga, Y, and Cu in olivine from the nine studied systems are listed in Table 1; the full sets of the LA-ICP-MS analysis data are presented in the online Supplementary Tables S1–S9. Vanadium concentrations in olivine are low relative to those in the emplaced komatiite and picrite lavas and vary in a narrow range, between 3.43 and 10.7 ppm, indicating incompatible behavior of V in olivine. Vanadium abundances in olivine within individual komatiite systems show differences in variability, from ~0.93% (2SD) in the Schapenburg system, up to ~24% in the Icelandic picrite system (Table 1). The average Sc abundances in olivine are slightly more variable, from ~6.8% (2SD) in the Winnipegosis system, up to ~42% in the Schapenburg system. The V/Sc ratios in the olivines vary from 0.69 ± 0.09 (2SD) in the Song Da system, up to 1.6 ± 0.4 in the Onega Plateau lavas. The Ga and Y concentrations in olivine are very consistent within a single system, but Cu concentrations are highly variable both within individual samples and between samples within the same komatiite/picrite system, possibly reflecting the presence of Cu-rich inclusions in olivine that are heterogeneously distributed within the flow, and/or remobilization of Cu during metamorphic alteration (Waterton et al., 2017). This conclusion is further supported by the instability of the Cu signal during LA-ICP-MS analyses compared to that of the other trace elements.

4.2. Trace metal abundances in the whole-rock samples

The abundances of V, Sc, Ga, Cu, Y, and Zr in the whole-rock samples from the nine komatiite and picrite systems are listed in Tables 2–4; the V abundances are also plotted as a function of MgO contents in Figs. 2–4.

Vanadium abundances (and also Ga and Sc – not shown) are strongly inversely correlated with MgO contents, thus exhibiting incompatible behavior over the entire range of compositions present in the studied lavas. These regression lines pass through the measured olivine compositions for each individual system, indicating that these regression lines represent olivine control lines. The Y abundances (not shown) display similarly incompatible well-constrained behavior in all but the Iceland picrites, where the Y data are more scattered (MSWD = 10). Cu and Zr plot with considerably more scatter, and show deviations from linear behavior in the Onega Plateau and

Table 1
Average trace metal abundances (in ppm) in olivine from the studied systems.

System	Sample	*N*	Sc	V	Cu	Ga	Y
Schapenburg	SCH1.10-1	34	3.69 ± 1.05	3.30 ± 1.04	1.93 ± 2.09	0.06 ± 0.05	0.15 ± 0.27
	SCH1.10-2	23	2.74 ± 0.83	3.32 ± 0.82	2.23 ± 1.90	0.06 ± 0.04	0.14 ± 0.25
Lapland	KD-05	50	4.70 ± 1.77	5.53 ± 1.88	3.76 ± 1.74	0.21 ± 0.09	0.08 ± 0.04
	KD-06	31	3.72 ± 0.65	5.76 ± 1.45	3.57 ± 1.16	0.20 ± 0.11	0.09 ± 0.03
	KD-08	36	3.87 ± 0.97	5.37 ± 1.83	2.83 ± 3.53	0.21 ± 0.10	0.08 ± 0.05
	KD-09	26	3.92 ± 1.30	5.49 ± 1.30	2.76 ± 3.22	0.23 ± 0.09	0.07 ± 0.04
	KD-10	15	3.67 ± 1.00	5.31 ± 0.81	2.52 ± 2.72	0.19 ± 0.07	0.07 ± 0.04
Onega Plateau	689-4	32	5.84 ± 1.85	10.0 ± 4.8	6.95 ± 5.06	0.30 ± 0.17	0.63 ± 0.51
	689-5	32	6.87 ± 1.51	10.6 ± 5.7	4.58 ± 6.05	0.31 ± 0.20	0.68 ± 0.46
Winnipegosis	RP1A-01	30	4.12 ± 0.57	4.71 ± 0.86	3.02 ± 3.25	0.25 ± 0.17	0.08 ± 0.03
	RP1A-02	32	4.27 ± 0.75	4.85 ± 0.87	1.85 ± 1.71	0.24 ± 0.12	0.08 ± 0.03
	RP1A-08	48	3.93 ± 0.69	4.84 ± 0.83	2.96 ± 2.48	0.18 ± 0.12	0.07 ± 0.03
	RP1A-11	48	4.05 ± 0.57	4.95 ± 0.89	3.11 ± 1.83	0.19 ± 0.12	0.07 ± 0.03
Song Da	VS 6-1-1	47	8.79 ± 2.46	5.67 ± 2.19	10.8 ± 6.5	0.31 ± 0.17	0.13 ± 0.08
	VS 6-1-2	32	7.73 ± 2.24	5.55 ± 2.50	12.6 ± 4.9	0.32 ± 0.23	0.12 ± 0.06
	VS 6-1-3	47	8.24 ± 2.35	5.83 ± 2.06	10.9 ± 5.5	0.28 ± 0.14	0.13 ± 0.10
Eastern Gorgona	GOR153-1	32	4.82 ± 0.86	6.98 ± 1.01	4.42 ± 0.57	0.35 ± 0.21	0.10 ± 0.04
	GOR153-2	46	5.66 ± 1.03	7.07 ± 0.93	4.49 ± 0.93	0.44 ± 0.29	0.12 ± 0.06
Western Gorgona	GOR538-1	47	6.69 ± 1.19	7.16 ± 1.12	4.54 ± 0.87	0.25 ± 0.10	0.13 ± 0.04
	GOR538-2	47	5.98 ± 0.91	7.07 ± 1.14	4.64 ± 1.51	0.23 ± 0.15	0.13 ± 0.04
	GOR538-3	47	6.38 ± 1.30	7.18 ± 1.17	4.56 ± 1.64	0.25 ± 0.09	0.13 ± 0.03
Padloping	AK-6	22	7.09 ± 1.03	10.1 ± 1.8	8.67 ± 1.65	0.23 ± 0.06	0.13 ± 0.04
	DB-9	31	6.58 ± 0.90	8.50 ± 2.25	6.93 ± 1.16	0.21 ± 0.09	0.12 ± 0.05
	PI-20	32	7.24 ± 1.63	9.18 ± 2.37	4.54 ± 1.59	0.21 ± 0.22	0.13 ± 0.12
Kilauea Iki	15H-1	30	5.73 ± 0.55	5.43 ± 0.73	3.86 ± 0.48	0.20 ± 0.08	0.13 ± 0.03
	15H-2	13	4.95 ± 0.72	5.57 ± 0.44	4.21 ± 1.67	0.25 ± 0.10	0.15 ± 0.05
	15H-3	31	6.09 ± 1.39	5.59 ± 0.82	3.82 ± 0.49	0.20 ± 0.06	0.11 ± 0.02
	15H-4	32	4.88 ± 1.06	5.64 ± 0.63	3.78 ± 0.29	0.17 ± 0.03	0.12 ± 0.03
Iceland	ICE4A	56	7.78 ± 2.34	5.06 ± 1.70	4.05 ± 1.45	0.16 ± 0.08	0.07 ± 0.03
	ICE4B	8	7.20 ± 0.70	5.35 ± 1.35	4.14 ± 0.30	0.19 ± 0.07	0.08 ± 0.02
	ICE5	16	6.14 ± 1.22	5.65 ± 1.35	4.30 ± 0.88	0.17 ± 0.05	0.06 ± 0.01

Note. *N* – number of olivine grains analyzed in each given sample. The uncertainties are 2SD. Data for the individual LA-ICP-MS analyses for each of the komatiite and picrite systems are provided in the online Supplementary Tables S1–S9.

Schapenburg systems for Cu, and the Padloping Island, Onega Plateau and Schapenburg systems for Zr. These deviations from olivine control lines for Y, Zr and Cu are most likely due to seafloor alteration and metamorphism, or fractionation of another significant phase hosting these elements in the systems, or both. These observations attest to the immobile behavior of V, Sc and Ga, the most petrogenetically important elements in this study, on the whole-rock scale (and also Y, Cu, and Zr in most cases) since crystallization of the studied systems and provide evidence for olivine being the only major fractionating phase that controlled variations in the abundances of these elements in the studied komatiite and picrite systems.

4.3. Estimation of the V and Sc abundances in the emplaced komatiite lavas

The FeO content, as well as the calculated MgO content, of each of the emplaced lavas are listed in Table 5, and errors on the emplaced MgO content of each system are propagated in quadrature to calculations of concentrations of incompatible elements in the emplaced lavas. The average maximum MgO and average minimum FeO contents in the liquidus olivine used to calculate the emplaced lava MgO content in each of the nine systems are listed in Table 6 and in the online Supplementary Tables S1–S9. The calculated MgO contents in the emplaced lavas vary between 21.1 ± 2.5 and 28.6 ± 2.8 wt.% in the Precambrian komatiite systems, then decrease to 7.95 ± 0.28 – 19.3 ± 1.6 wt.% in the picrite and Phanerozoic komatiite systems.

Using the calculated MgO contents in the emplaced lavas for each system and regressing the trace element abundance data obtained in this study for the whole-rock samples and olivine against the MgO contents using ISOPLOT (Ludwig, 2003), Sc and V abundances in the emplaced komatiite lavas for each individual komatiite system have been calculated; these abundances, with their respective propagated 2SD uncertainties, are also presented in Table 5. The calculated V and Sc abundances vary from 115 ± 18 to 278 ± 12 and 17.8 ± 2.3 to 40.3 ± 2.6 ppm,

Table 2
Trace metal abundances in whole-rock samples from the Schapenburg, Lapland, and Onega Plateau systems.

System	Sample	MgO	LOI	Sc	V	Cu	Ga	Y	Zr	Lithology
Schapenburg	SCH1.1	26.5	4.15	19.2	138	319	5.47	6.91	10.3	Ol spx
	Replicate			19.4	139	313	5.44	6.99		
	SCH1.2	27.9	5.12	17.8	117	35.8	5.03	6.28	11.0	Ol spx
	Replicate			17.5	115	34.8	5.02	6.16		
	SCH1.3	26.7	3.52	19.2	126	94.8	5.20	7.12	14.0	Ol spx
	Replicate			19.2	126	94.8	5.16	7.07		
	SCH1.4	26.9	3.39	20.2	125	26.9	5.30	7.08	10.7	Ol spx
	Replicate			20.2	125	26.9	5.26	7.07		
	SCH1.5	25.9	2.80	19.3	130	152	5.41	7.27	11.4	Ol spx
	Replicate			19.3	130	151	5.36	7.12		
	SCH1.6	24.8	2.48	20.6	151	301	5.54	7.90	15.0	Ol spx
	SCH1.8	28.7	4.13	18.5	120	2.14	4.42	6.76	7.64	CM
	Replicate			18.2	123	2.17	4.33	6.74		
	SCH1.9	32.3	7.09	14.8	91.7	0.598	3.65	5.12	9.86	Ol cum
	Replicate			14.9	90.9	0.811	3.73	5.30		
	Replicate			14.9	91.6	0.718	3.63	5.10		
	SCH.10	36.0	8.27	12.6	78.4	0.593	3.18	4.03	8.04	Ol cum
	Replicate			12.6	78.0	0.867	3.16	4.04		
	Replicate			12.7	78.7	0.850	3.22	4.07		
Lapland	KD-05	22.6	0.63	30.4	238	114	11.8	10.9	31.9	KD
	KD-06	22.3	0.55	29.3	228	111	11.5	10.7	30.0	KD
	KD-08	25.2	1.40	26.6	210	104	10.5	9.36	27.3	KD
	KD-09	28.3	1.47	24.9	172	86.0	8.52	7.50	19.3	KD
	KD-10	28.3	2.15	25.3	180	7.26	8.50	7.41	21.0	KD
	KD-11	24.2	1.25	28.4	223	108	11.1	10.0	29.3	KD
	KD-12	21.2	1.01	31.2	255	119	12.6	11.9	35.2	KD
	KD-13	20.2	1.22	31.7	258	123	12.9	11.9	36.5	KD
Onega Plateau	689-1	21.7	6.11	24.5	250	60.5	13.6	12.9	83.6	Pic
	689-3	30.6	8.19	19.4	160	104	7.56	7.83	46.8	Pic
	689-4	31.2	7.74	18.4	143	90.8	7.38	8.38	50.5	Pic
	689-5	31.7	7.61	19.1	147	68.9	6.85	7.22	39.9	Pic
	689-6	29.5	7.70	23.0	162	147	7.69	7.72	44.0	Pic
	9702	13.6	5.30	28.3	340	114	17.1	19.7	124	Pic
	9704	29.3	7.30	20.8	164	232	7.52	7.41	43.2	Pic
	9705	30.3	7.95	22.4	170	243	7.81	7.88	44.7	Pic

Note. Here and in Tables 3 and 4, the abundances of both MgO (wt.%) and trace metals (ppm) are re-calculated on an anhydrous basis using measured LOI (wt.%) values. CM – chilled margin, Ol spx – olivine spinifex, Ol cum – olivine cumulate, Pic – picrite, KD – komatiitic dike. The rest of the major element data are provided in the online Supplementary Tables S1–S9.

Table 3
Trace metal abundances in whole-rock samples from the Winnipegosis, Song Da and Gorgona Island komatiite systems.

System	Sample	MgO	LOI	Sc	V	Cu	Ga	Y	Zr	Lithology
Winnipegosis	RP1A-01	24.2	2.93	27.1	n.d.	73.3	9.06	9.67	25.0	MK
	RP1A-04	20.3	3.73	29.2	211	83.7	10.5	10.9	29.3	MK
	RP1A-05	23.0	3.24	28.6	193	80.2	9.56	10.2	26.6	MK
	RP1A-08	25.3	3.05	26.2	177	72.6	8.72	9.19	24.1	MK
	RP1A-09	22.0	2.70	29.5	197	82.2	9.87	10.5	27.6	MK
	RP1A-11	24.0	2.36	26.2	183	75.2	9.09	9.40	25.1	MK
	RP1A-12	22.8	2.54	27.5	196	83.1	9.56	10.0	26.3	MK
	RP1A-14	21.4	4.31	30.5	205	n.d.	10.0	10.9	28.2	MK
	RP1A-17	20.6	4.12	30.3	204	92.6	10.1	11.0	29.5	MK
Song Da	P 9/86	26.8	5.25	27.2	180	81.7	8.77	10.2	17.7	MK
	Replicate			27.0	177	82.7	8.87	10.0	17.5	MK
	P 11/86	32.6	8.55	23.1	140	61.5	7.27	8.30	17.1	MK
	Replicate			21.9	139	59.1	7.09	8.04	16.3	MK
	B6887	33.5	6.33	21.6	122	59.9	6.22	7.83	14.3	Ol cum
	Replicate			22.0	122	56.8	6.18	7.83	13.4	Ol cum
	VS 5-1	21.4	3.96	34.8	227	114	12.0	14.4	24.4	MK
	Replicate			31.8	237	121	12.0	14.7	24.1	MK
	VS 6-1	22.6	2.23	33.0	207	100	11.0	13.6	22.8	Ol cum
	Replicate			31.7	214	112	11.4	13.8	22.7	Ol cum
	VS 6-2	14.3	4.55	43.2	261	45.7	14.5	15.8	27.0	MK
	Replicate			40.3	251	47.4	13.9	15.0	25.5	MK
Eastern Gorgona	GOR152	15.3	2.80	37.7	307	146	14.6	15.3	33.1	CM
	GOR153	23.8	3.29	29.3	227	107	10.9	11.4	24.8	Ol cum
	GOR155	15.4	5.97	38.9	314	155	14.4	15.6	31.9	Ol spx
	GOR156	17.7	3.09	35.0	284	134	13.6	14.3	30.9	Ol spx
	GOR157	12.1	3.15	42.0	346	158	16.3	17.3	36.5	Ol spx
	GOR159	18.7	2.69	34.2	276	133	13.4	13.8	29.2	Ol spx
	GOR160	17.8	5.07	35.7	289	132	14.0	14.4	30.9	Ol spx
Western Gorgona	GOR537	17.2	1.83	35.2	293	137	13.8	14.5	29.9	Ol spx
	GOR538	25.7	2.88	27.3	221	99.5	10.1	10.4	21.8	Ol cum
	GOR539	18.3	4.21	33.3	266	135	13.0	13.4	28.2	Ol spx
	GOR540	18.0	4.64	36.6	298	123	13.2	13.2	26.4	Ol spx

Note. CM – chilled margin, Ol spx – olivine spinifex, Ol cum – olivine cumulate, MK – massive komatiite. Additional major element data are provided in the online Supplementary Tables S1–S9. n.d. – no data.

Table 4
Trace metal abundances in whole-rock picrite samples from the Kilauea Iki lava lake, the Western Rift Zone of Iceland, and Padloping Island.

System	Sample	MgO	LOI	Sc	V	Cu	Ga	Y	Zr	Lithology
Kilauea Iki	H15-1_1	11.7	−0.48	29.7	311	119	19.7	22.0	150	MP
	Replicate			30.1	309	126	19.3	22.0	148	MP
	15H-1_2	11.6	−0.48	30.3	310	124	19.5	22.1	151	MP
	H15-2_1	17.6	−0.39	25.8	259	106	16.2	18.4	124	MP
	15H-2_2	17.8	−1.50	25.0	248	106	15.7	17.7	120	MP
	H15-3_1	12.1	−0.50	29.5	301	106	19.0	20.7	145	MP
	Replicate			29.7	305	107	19.3	21.4	148	MP
	15H-3_2	12.4	−0.47	29.8	304	111	19.0	21.4	148	MP
	H15-4_1	15.7	−0.56	26.4	275	107	17.2	19.1	129	MP
	15H-4_2	16.3	−0.54	26.9	273	105	17.0	19.0	130	MP
Iceland	ICE4A	25.3	n.d.	34.2	191	72.3	9.40	8.91	15.3	MP
	ICE4B	23.9	n.d.	35.0	200	71.3	9.69	9.04	15.4	MP
	ICE5	18.8	n.d.	38.1	225	83.0	11.8	9.67	14.0	MP
	Replicate	18.8	n.d.	38.6	224	83.1	11.9	9.80	14.0	MP
Padloping	AK-6	25.0	2.73	28.7	200	92.8	9.96	11.6	26.1	MP
	DB-9	23.0	1.41	30.0	216	99.3	10.9	12.6	34.9	MP
	PI-20	19.5	0.79	36.1	249	93.3	12.4	15.3	45.9	MP

Note. The remainder of the major element data are provided in the online Supplementary Tables S1–S9. MP- massive picrite. n.d. – no data.

respectively, in the komatiite systems, and 238 ± 12 to 404 ± 19 and 27.5 ± 0.7 to 40.5 ± 2.2 ppm, respectively, in the picrite systems.

4.4. Evaluation of the redox state of the komatiite and picrite systems

4.4.1. Vanadium and Sc partitioning between olivine and emplaced lavas

The average V and Sc concentrations in the liquidus olivine, with their respective propagated 2SD uncertainties, are presented in Table 6. Using these values and the estimated V and Sc abundances in the emplaced komatiite lavas (Table 5), partition coefficients for V and Sc between liquidus olivine and emplaced lavas for the studied komatiite and picrite systems were obtained; these data are listed in Table 6 and presented in the MgO vs. V variation diagrams (Figs. 2–4). Uncertainties on the komatiite lava and average olivine compositions were propagated in quadrature to determine the uncertainties on the $D_V^{Ol\text{-}Liq}$ for the individual systems.

The calculated $D_V^{Ol\text{-}Liq}$ values do not show any correlation with the petrologic types of the lavas studied (*e.g.,* komatiite or picrite). However, the *D* values do exhibit a trend with age of the systems, decreasing from 0.0284 ± 0.0034 in the 2.06 Ga Lapland komatiite system to 0.0207 ± 0.0021 and 0.0199 ± 0.0007 in the 251 Ma Song Da and modern Kilauea Iki systems, respectively. The $D_{Sc}^{Ol\text{-}Liq}$ values range between 0.135 ± 0.015 and 0.205 ± 0.030 and do not appear to exhibit any secular trend, possibly varying as a result of temperature or melt composition effects.

Having determined the V partition coefficients between the liquidus olivine and the emplaced lavas for the nine systems, we used the combined experimental calibrations of Canil (1997) and Canil and Fedortchouk (2001) to evaluate the oxidation states of these komatiite and picrite systems. Regressions of experimental data compiled by Nicklas et al. (2018) from the above two publications yielded the following equation:

$$\log\left(D_v^{Ol-Liq}\right) = (-0.250 \pm 0.023) \times \Delta NNO - (1.501 \pm 0.064)\ (r^2 = 0.94) \quad (1)$$

Uncertainties on the slopes and intercepts of Eq. (1) were derived from the 95% confidence interval of the regression of the experimental data and experimental uncertainties using ISOPLOT 3.00 (Ludwig, 2003). The uncertainties shown in Eq. (1) were propagated in quadrature through the determination of fO_2 from $D_V^{Ol\text{-}Liq}$. More information on the experimental regression shown in Eq. (1) can be found in Nicklas et al. (2018).

Although V partitioning oxybarometers that take into account abundances of other major elements, mostly alkalis, in the crystallizing melt do exist (e.g., Mallmann and O'Neill, 2009, 2013), those oxybarometers are not applicable to samples that experienced seafloor alteration and/or metamorphism, for which the primary abundances of fluid-mobile major elements (such as the alkalis) are difficult to constrain. Although the abundances of fluid-mobile elements are well constrained in some of the

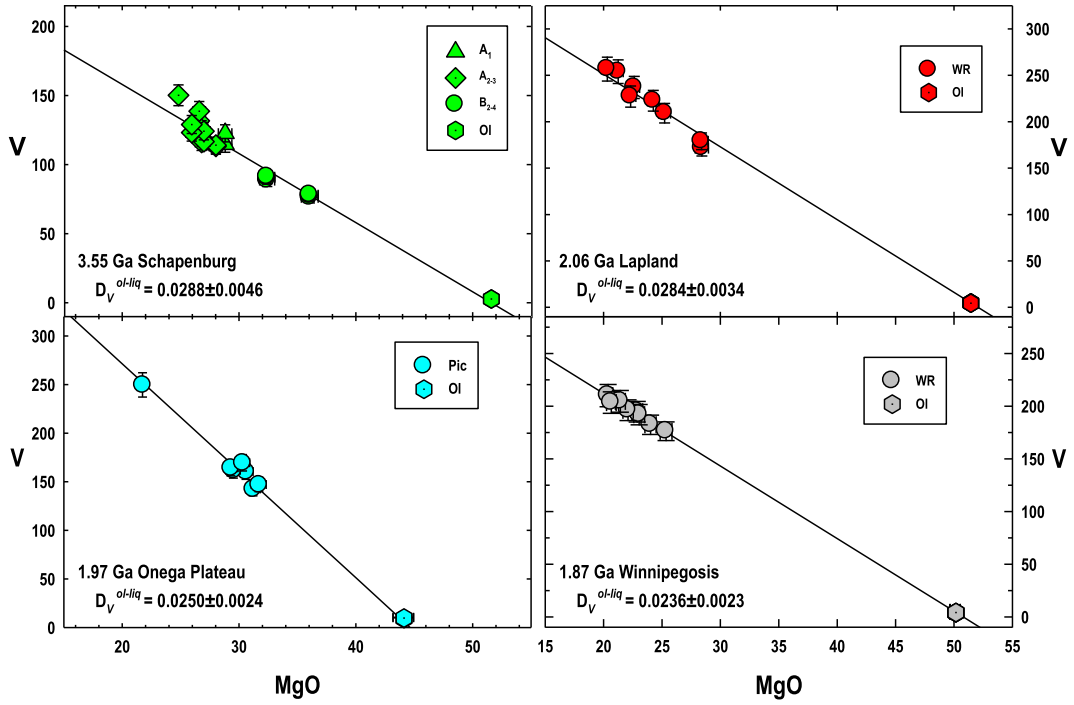

Fig. 2. Vanadium (ppm) abundances in whole-rock samples and olivine from the 3.55 Ga Schapenburg komatiite, 2.06 Ga Lapland komatiite, 1.97 Onega Plateau picrite, and 1.87 Ga Winnipegosis komatiite systems plotted against MgO contents (wt.%). A_1 – upper chilled margin, A_{2-3} – spinifex zone, B_{2-4} – cumulate zone, WR – whole rock, and Ol – olivine. The composition of the upper chilled margin zone approximates that of the emplaced lava. The details of the protocol for calculating the $D_V^{Ol\text{-}Liq}$ values for each system here and in Figs. 3 and 4 are given in the text. The uncertainties here and in Figs. 3 and 4 are propagated 2SD uncertainties.

younger systems, there exists a systematic offset between the fO_2 values calculated using different oxybarometers (Mallmann and O'Neill, 2013) and as such, we have chosen to use only partitioning data from a single suite of experiments. As the experiments of Canil (1997) and Canil and Fedortchouk (2001) used bulk compositions close to that of the lavas studied here we have elected to use those experimental data. The composition-independent oxybarometer in Eq. (1) is derived from those data, and is used to facilitate comparison between the Archean and modern lavas. For ease of comparison to previously published data for mantle-derived rocks, all of the oxygen fugacity values have been converted from ΔNNO log units to the more commonly used ΔFMQ log units using the standard thermodynamic values for each mineral buffer assemblage listed in Wood (1991). The fO_2 values calculated from the V partitioning data are listed in Table 6 and plotted as a function of the age of the studied systems in Fig. 5a.

The early Archean Schapenburg komatiite system is characterized by an elevated calculated fO_2 value of $+0.88 \pm 0.38$ ΔFMQ log units, significantly higher than the spatially and temporally associated 3.48 Ga Komati system at -0.11 ± 0.30 ΔFMQ log units (Nicklas et al., 2018). The Schapenburg system has been found to retain short lived ^{182}W and ^{142}Nd isotope anomalies (Puchtel et al., 2016a), while no such anomalies have been detected in the Komati system (Touboul et al., 2012). The Schapenburg system, therefore, likely sampled a region of the mantle that was anomalous with respect to both fO_2 and short-lived isotope systems, and, thus, does not represent the bulk of the mantle at 3.55 Ga. The lavas from the Padloping Island picrite system show the lowest measured fO_2 value at $+0.60 \pm 0.41$ ΔFMQ, which is within uncertainty of that estimated in the related Anaanaa unit of West Greenland at ~+0.28 ΔFMQ (Larsen and Pedersen, 2000). The Padloping lavas have also been shown to have large short-lived isotopic anomalies (Rizo et al., 2016) and were, therefore, also not used to characterize the mantle at 62 Ma. The significance of the obtained fO_2 values for these two systems is further addressed in Section 5.4.

The fO_2 values of the remaining komatiite and picrite systems vary between $+0.90 \pm 0.33$ ΔFMQ in the Lapland system, to $+1.52 \pm 0.27$ ΔFMQ in the Kilauea Iki system, and show a broad correlation with age. Data from this study, combined with the Archean komatiite data from Nicklas et al. (2018), define a secular trend in oxygen fugacity from 3.48 Ga to the present day, with an overall change in oxidation state of ~1.6 log units. The change is most marked from 3.48 to 1.87 Ga, with all systems postdating the Winnipegosis system having fO_2 values that are identical within errors. A linear least-squares ISOPLOT regression (MSWD = 2.4) of the fO_2 data from 3.48 to 1.87 Ga yields a slope of 0.80 ± 0.20 log units ΔFMQ /Ga. This linear regression is plotted in Fig. 5a. The difference in oxygen

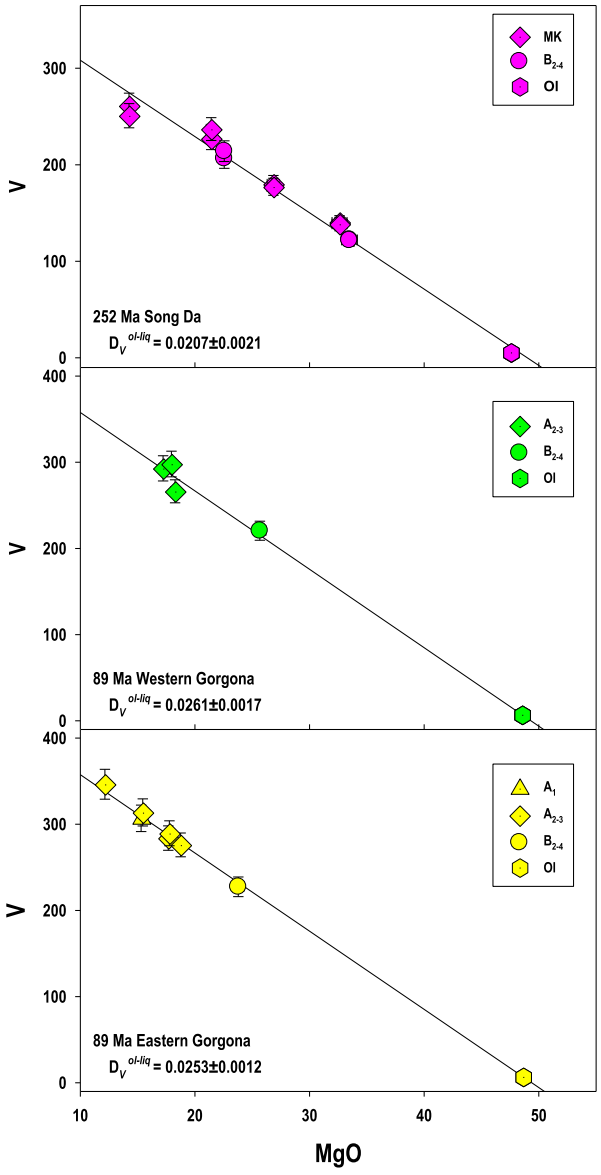

Fig. 3. Vanadium (ppm) abundances in komatiite whole-rock samples and olivine from the 251 Ma Song Da komatiite system and from two flows of the 89 Ga Gorgona komatiite system plotted against MgO contents (wt.%). A_1 – upper chilled margin, A_{2-3} – spinifex zone, B_{2-4} – cumulate zone, MK – massive komatiites, and Ol – olivine.

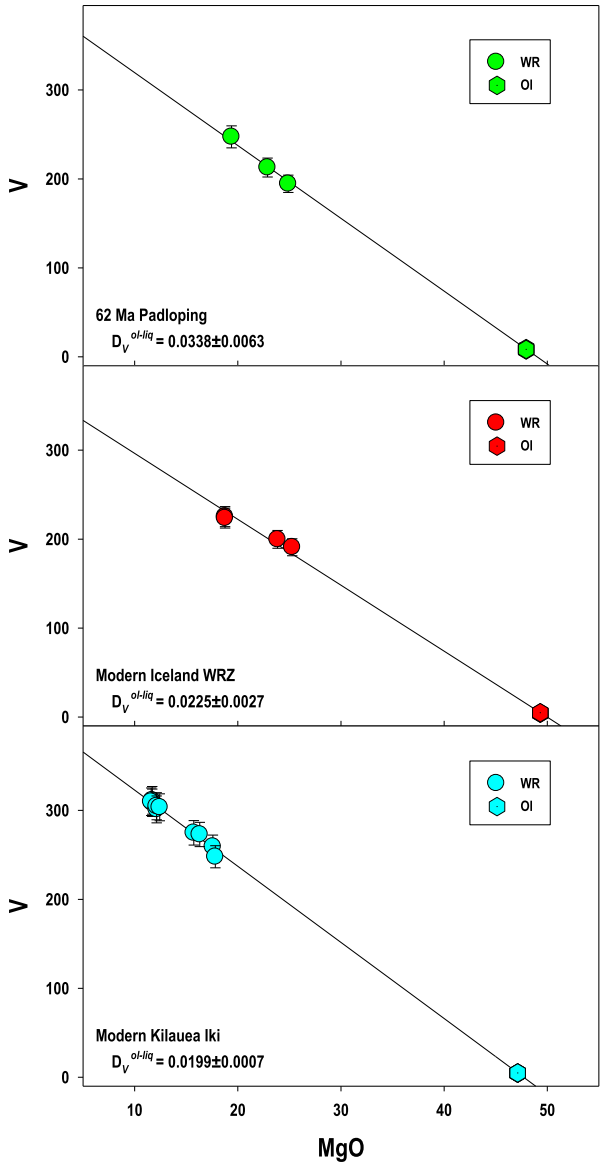

Fig. 4. Vanadium (ppm) abundances in whole-rock samples and olivine from the 62 Ma Padloping Island picrites, as well as picrites from the 1959 eruption of Kilauea Iki and the Western Rift Zone (WRZ) of Iceland plotted against MgO contents (wt.%). WR – whole rock, Ol – olivine.

fugacity between the Komati and Winnipegosis systems, which anchor the ends of the linear regression line, is 1.33 ± 0.43 log units.

Also plotted in Fig. 5a is an estimate of the redox state for modern East Pacific Rise MORB obtained using V abundance data of the olivine-glass pairs from Kelley and Cottrell (2012) and Mallmann and O'Neill (2013) and Eq. (1) above at $+0.60 \pm 0.15$ ΔFMQ log units (2SD). It has been shown that the redox data obtained using oxybarometers relying on the partitioning behavior of V are systematically offset by up to 1 log unit from the oxygen fugacity data obtained using the $Fe^{3+}/\Sigma Fe$ equilibria (e.g., Mallmann and O'Neill, 2013), so only MORB data determined using the same method as for the samples studied here are used for comparison. As most modern MORB are erupted at or close to sulfide saturation (Bottinga and Javoy, 1990; Le Voyer et al., 2015), and sulfur degassing can affect the redox state of a lava (Moussallam et al., 2014), the calculated MORB average likely represents a minimum fO_2 estimate. It is, thus, not surprising that the MORB average plots below most of the Phanerozoic systems studied. For more information on the calculations of the MORB average plotted in Fig. 5a the reader is referred to Nicklas et al. (2018).

Table 5
The measured FeO and calculated MgO abundances (wt.%), along with calculated V, and Sc abundances (ppm) and V/Sc ratios in emplaced lavas from the studied komatiite and picrite systems.

	FeO	MgO	V (ppm)	Sc (ppm)	V/Sc
Schapenburg	11.7	28.6 ± 2.8	115 ± 18	17.8 ± 2.3	6.47 ± 1.34
Lapland	11.3	27.4 ± 2.4	193 ± 19	25.4 ± 2.4	7.60 ± 1.04
Onega Plateau	9.00	7.95 ± 0.28	411 ± 23	38.9 ± 8.7	10.6 ± 2.4
Winnipegosis	11.4	21.1 ± 2.5	205 ± 18	29.6 ± 2.4	6.91 ± 0.82
Song Da	11.4	14.3 ± 1.0	274 ± 25	40.3 ± 2.6	6.80 ± 0.75
Eastern Gorgona	11.4	18.8 ± 1.1	278 ± 12	34.5 ± 1.7	8.04 ± 0.53
Western Gorgona	11.4	19.3 ± 1.6	273 ± 17	33.4 ± 2.2	8.17 ± 0.73
Padloping	10.4	15.5 ± 1.4	274 ± 15	37.5 ± 2.4	7.31 ± 0.62
Kilauea Iki	11.4	15.0 ± 0.6	280 ± 5	27.5 ± 0.7	10.2 ± 0.3
Iceland	11.4	17.9 ± 1.3	238 ± 12	40.5 ± 2.2	5.88 ± 0.44

Note. The background data and the calculation details are provided in the text and in the online Supplementary Tables S1–S9. The V and Sc abundances in the emplaced komatiite lavas and the uncertainties on the V and Sc abundances were derived from ISOPLOT regression calculations and are propagated 2SD uncertainties.

4.4.2. Variations in V/Sc in the emplaced komatiite and picrite lavas

Variations in V/Sc ratios in Archean basalts as a function of age have been used to study the evolution of the oxidation state of the Archean upper mantle (e.g., Li and Lee, 2004). Because V becomes more incompatible with an increase in fO_2 of the system, and Sc partitioning is independent of fO_2, the higher the fO_2 of the system during melting, the higher the V/Sc ratio should be in the melt. Li and Lee (2004) estimated the V/Sc in the global compilation of MORB lavas to be 6.7 ± 1.1 (2SE), which is equivalent to −0.3 ± 1.0 ΔFMQ log units for the modern upper mantle. They also estimated that Archean basalts have an average V/Sc = 6.3 ± 1.2 (2SE) and concluded that the fO_2 of the modern upper mantle and that of the sources of Archean basalts were identical within the cited uncertainties.

We applied the V/Sc oxybarometer of Li and Lee (2004) to the komatiite and picrite systems from this study, by calculating the V/Sc ratios in the emplaced lavas of each system. The V/Sc ratios vary from 5.88 ± 0.44 in the Icelandic picrites to 10.2 ± 0.3 in Kilauea Iki lava lake. These V/Sc ratios, along with those determined for Archean komatiites in Nicklas et al. (2018), as well as the MORB range from Li and Lee (2004), are plotted against age in Fig. 5b. No significant trend is observed, and all but the Kilauea Iki and Onega Plateau lavas plot within the range of modern MORB. The data obtained using the V/Sc oxybarometer, thus, provide no evidence for secular oxidation within our sampled systems. Similar oxybarometers utilizing the V/Ga and V/Y ratios (Mallmann and O'Neill, 2013; Laubier et al., 2014) also show no variation in the calculated fO_2 with time. The reasons for this and the implicit assumptions behind these oxybarometers are discussed below.

Firstly, it is important to note that since komatiites and picrites are high melt-fraction lavas, they are expected to show less variation in V/Sc as a function of oxygen fugacity than basalts, with their V/Sc ratios being closer to those of their mantle source regions. Another complicating factor is the difference in melting histories of different komatiite and picrite systems, as the use of V/Sc as an oxybarometer relies on the assumption that the V/Sc in the source region of all the studied rocks was identical. However, previous melt depletion events at high oxygen fugacity would lower the V/Sc ratio of a mantle source region, leading to subsequent melts extracted from that source to give erroneously reduced values using this oxybarometer. Finally, V^{3+} and Sc^{3+} behave similarly during melting in the spinel stability field, but may have significantly different partition coefficients between solid and melt in the garnet stability field. Petrologic modeling has shown that melting in the garnet stability field will indeed impart a higher V/Sc ratio at constant fO_2 when compared to melting in the spinel stability field (Lee et al 2005; Aulbach and Stagno, 2016). Notably, the Kilauea Iki and Onega Plateau systems have much higher V/Sc ratios, at 10.2 ± 0.3 and 10.0 ± 1.7, respectively, than any of the other systems. It has been previously determined that both systems are primarily the result of melting in the garnet stability field (Puchtel et al., 1998a; Norman and Garcia, 1999), illustrating the possible effect of residual garnet on the V/Sc ratio of the melt. Due to these limitations, we did not consider any further the V/Sc systematics of the studied komatiite and picrite systems for the purpose of constraining their redox state.

5. DISCUSSION

5.1. The effects of alteration, mineral-melt re-equilibration, and crustal contamination on the redox state of the studied komatiite systems

5.1.1. Secondary alteration

The effect of secondary alteration on the determination of fO_2 of Archean komatiites has been previously addressed by Nicklas et al. (2016, 2018). Additionally, the effect of surface alteration on the chemistry of the Schapenburg komatiite flows has been previously addressed in Puchtel et al. (2016a). The Phanerozoic and Proterozoic samples studied here are mineralogically very well preserved, and metamorphic grade was uniformly sub-greenschist facies. Igneous textures are preserved in all of the studied

Table 6
Average maximum MgO and minimum FeO (wt.%) and average V and Sc abundances in liquidus olivine and calculated D_v and D_{Sc} and fO_2 in the systems studied.

Locality	MgO	FeO	V (ppm)	Sc (ppm)	$D_v^{Ol\text{-}Liq}$	$D_{Sc}^{Ol\text{-}Liq}$	fO_2 (ΔNNO)	fO_2(ΔFMQ)
Schapenburg	51.54 ± 0.54	6.32 ± 0.50	3.31 ± 0.03	3.22 ± 1.34	0.0288 ± 0.0046	0.181 ± 0.079	0.16 ± 0.38	0.88 ± 0.38
Lapland	51.38 ± 0.55	6.43 ± 0.32	5.49 ± 0.35	3.98 ± 0.84	0.0284 ± 0.0034	0.156 ± 0.036	0.18 ± 0.33	0.90 ± 0.33
Onega Plateau	44.06 ± 0.47	15.46 ± 0.37	10.29 ± 0.83	6.35 ± 1.46	0.0250 ± 0.0024	0.163 ± 0.053	0.40 ± 0.31	1.12 ± 0.31
Winnipegosis	50.10 ± 0.44	8.13 ± 0.63	4.84 ± 0.20	4.09 ± 0.28	0.0236 ± 0.0023	0.138 ± 0.015	0.50 ± 0.31	1.22 ± 0.31
Song Da	47.55 ± 0.35	11.36 ± 0.38	5.68 ± 0.28	8.26 ± 1.06	0.0207 ± 0.0021	0.205 ± 0.030	0.73 ± 0.32	1.45 ± 0.32
Eastern Gorgona	48.62 ± 0.31	8.86 ± 0.26	7.02 ± 0.13	5.24 ± 1.19	0.0253 ± 0.0012	0.152 ± 0.035	0.38 ± 0.27	1.10 ± 0.27
Western Gorgona	48.53 ± 0.52	8.64 ± 0.39	7.14 ± 0.12	6.35 ± 0.71	0.0261 ± 0.0017	0.190 ± 0.025	0.33 ± 0.28	1.05 ± 0.28
Padloping	47.89 ± 0.56	10.96 ± 0.58	9.27 ± 1.64	6.94 ± 0.81	0.0338 ± 0.0063	0.185 ± 0.025	−0.12 ± 0.41	0.60 ± 0.41
Kilauea Iki	47.07 ± 0.15	11.15 ± 0.15	5.56 ± 0.19	5.41 ± 1.19	0.0199 ± 0.0007	0.196 ± 0.044	0.80 ± 0.27	1.52 ± 0.27
Iceland	49.26 ± 0.33	9.42 ± 0.39	5.36 ± 0.59	7.04 ± 1.66	0.0225 ± 0.0027	0.174 ± 0.042	0.59 ± 0.34	1.31 ± 0.34

Note. The $D_v^{Ol\text{-}Liq}$ and fO_2 values were calculated using the protocol detailed in the text. All the uncertainties are the 2SD uncertainties propagated in quadrature.

Phanerozoic samples, and igneous minerals are very well preserved in the Song Da, Kilauea Iki, Gorgona, Iceland and Padloping lavas. The Schapenburg komatiite system and the Onega Plateau picrites are remarkably well preserved given their age, and the Lapland and Winnipegosis komatiite systems retain almost exclusively igneous minerals with little evidence for any secondary phases, indicating an excellent degree of preservation (Fig. 1).

Secondary alteration may result in re-distribution of petrogenetically important elements, including V, which, in turn, may have affected the estimates for V (and other trace metals) abundances in the emplaced lavas. This post-magmatic re-distribution on a whole-rock scale, however, can be easily recognized in the trace metal vs. MgO variation diagrams (Figs. 2–4). Element mobility will result in the data for the affected element plotting off the olivine control lines, which is not observed. Vanadium and Sc exhibit strong inverse correlations with MgO, with MSWD < 3.0 for all systems along with MgO intercepts close to the composition of liquidus olivine phenocrysts, and it is, thus, concluded that all komatiite and picrite systems retain primary, igneous distributions of these elements.

5.1.2. Late-stage re-equilibration of the liquidus olivine with host lava

The method we used to determine the redox state of the komatiite and picrite systems assumes that olivine was in chemical equilibrium with the emplaced lava. Although olivine phenocrysts found in chilled margins of komatiite lava flows most likely preserved their original V partitioning signature due to the almost instantaneous solidification after emplacement (Huppert et al., 1984; Huppert and Sparks, 1985; Arndt, 1986b), olivine from cumulate zones, which take much longer to crystallize, may have experienced re-equilibration with the residual liquid. In their study of the ~100-m-deep Victoria's lava lake, Nicklas et al. (2016) demonstrated that V contents of olivine from the cumulate zone and the upper chilled margin of the komatiitic lava lake were indistinguishable, which was taken as evidence that V re-equilibration between olivine and the residual liquid played a negligible role during the evolution of the lava lake. All samples, except for those from the Lapland, Onega Plateau, Kilauea Iki and Iceland systems, are from sub-aqueously erupted flows significantly thinner than the 100-m-deep lava lake, and thus re-equilibration was likely also negligible. The Lapland samples are sub-volcanic in nature, but still likely cooled relatively quickly, as the width of the Kevitsa dike from which they were collected was ~40 m. Similarly, the Onega Plateau samples analyzed come from the sub-volcanic Konchozero sill, which shows evidence for rapid solidification and cooling (Puchtel et al., 1998b). The samples from the Kilauea Iki and Iceland systems are sub-aerially erupted lavas that cooled quickly, albeit likely not as quickly as sub-aqueously erupted lavas, and thus also had little time for re-equilibration. In order to minimize the effect of re-equilibration, Kilauea Iki samples were taken from the upper chilled margin of the lava lake, which must have solidified rapidly. It is therefore likely that the olivine grains analyzed in this study retain their liquidus V and Sc concentrations in all the studied systems.

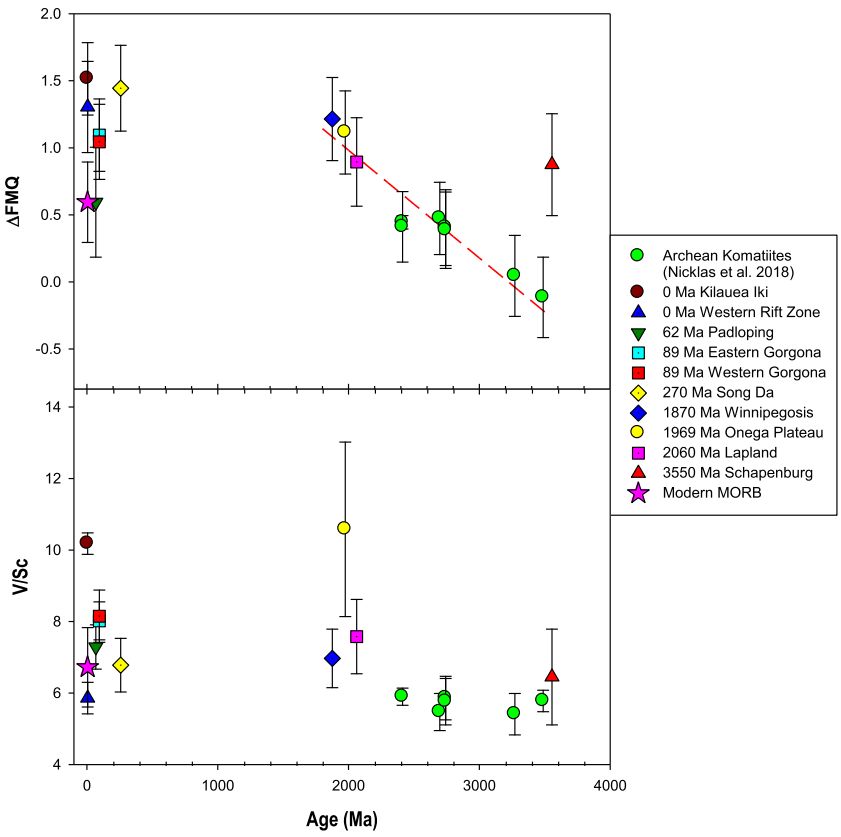

Fig. 5. (A) The calculated oxygen fugacity (fO_2) relative to the FMQ buffer for the studied komatiite and picrite systems plotted as a function of their ages. The uncertainties shown are determined by the propagated 2SD uncertainties on the calculated $D_V^{Ol\text{-}Liq}$ and the 95% confidence interval error of Eq. (1) in the text. The fO_2 estimates for modern MORB were calculated using the V partitioning of four olivine/glass pairs from Kelley and Cottrell (2012) and Mallmann and O'Neill (2013). The MORB value of $+0.60 \pm 0.30$ ΔFMQ log units is the average of the four estimates with the uncertainty reflecting the 2SD of those estimates propagated to account for the uncertainty in experimental calibrations in Eq. (1). The dotted red line is an ISOPLOT least-squares regression of all data from 3.48 to 1.87 Ga (MSWD = 2.4). See text for further details. (B) The V/Sc ratios of the studied komatiite and picrite systems plotted as a function of their ages. Data for modern MORB are from Li and Lee (2004). See text for additional details. (For interpretation of the references to color coding in this figure legend, the reader is referred to the web version of this article.)

5.1.3. Crustal contamination

Crustal contamination can have an effect on the fO_2 of mantle-derived lavas due to assimilation of oxidized species in continental crust that was generated in an oxidized arc environment. The Gorgona, Kilauea Iki and Iceland lavas are all known to have erupted in an oceanic environment and are thus not contaminated by continental crust. Of the komatiitic and picritic systems studied here that erupted onto continental crust, previous studies have found minimal crustal contamination, ranging from <1% in the Padloping Island picrites (Day, 2016), to 1–2% in the Song Da system (Hanski et al., 2004) to <3% in the Winnipegosis system (Waterton et al., 2017). The upper Onega Plateau picrites show no evidence for contamination with continental crust (Puchtel et al., 1998b). The degree of crustal contamination of the Lapland samples is also likely very low, as shown by their εNd values ranging from +3 to +4 and their strong depletion in LREE (Huhma et al., 2018). Based on their trace element and Nd isotopic systematics, it is also unlikely that the Schapenburg komatiites experienced any crustal contamination (Puchtel et al., 2009). In addition, the study of Grocke et al. (2016) observed no effect on fO_2 in continental arc lavas that had been variably contaminated by up to >30% continental crust, and, thus, it is unlikely that the low degree of contamination found in all of the studied systems had a measurable effect on the calculated fO_2 values.

5.2. The significance of the calculated fO_2 of the studied komatiite systems

5.2.1. The effect of temperature on V partitioning in ultramafic systems

The experimental studies of Mallmann and O'Neill (2013) and Laubier et al. (2014) showed a dependence of $D_V^{ol/melt}$ on the temperature of olivine crystallization. As the younger suites analyzed have, on average, lower liquidus temperatures, it is important to evaluate the effect of temperature on the partitioning of V in the komatiitic and picritic lavas studied. A decrease in temperature of ca. 100 °C would result in a change of ~0.1 log unit in the

calculated oxygen fugacity using the Mallmann and O'Neill (2013) oxybarometer, which takes temperature into account. Although our suites show a large range in the emplaced lava MgO contents (7.95–28.6 wt.% MgO), this spread likely corresponds to a maximum of 400 °C difference in the liquidus temperatures. A 0.4 log unit oxidation is significantly smaller than the observed range of ~1.6 log units. Furthermore, the MgO content of the lavas, a proxy for liquidus temperature, does not show a correlation with the calculated oxygen fugacity, as the lowest MgO samples from the Onega Plateau, at 7.95 wt.% MgO, have an fO_2 within uncertainty of those of the Lapland and Winnipegosis komatiites, which contained 27.4 and 21.1 wt.% MgO in their emplaced lavas, respectively, encompassing almost the entire spectrum of the MgO contents of the sample set, with minimal changes in fO_2.

5.2.2. The effect of mantle secular cooling on fO_2

It is generally accepted that the mantle has experienced secular cooling (Herzberg et al., 2010; Ganne and Feng, 2017; Aulbach and Arndt, 2019); as such, the older komatiite systems likely formed from a hotter mantle than their younger counterparts. In order to evaluate the significance of the calculated fO_2 of the studied komatiite systems, it is important to constrain the effects of secular cooling of the mantle (e.g., Nisbet et al., 1993; Herzberg et al., 2010) on the calculated oxygen fugacities. Decrease in mantle temperatures will result in increased Fe^{3+} activity in mantle spinel, and, thus, higher mantle oxygen fugacity in the spinel peridotite stability field due to the temperature dependence of mantle mineral redox equilibria (Ballhaus et al., 1991). The extent to which the mantle cooled over the past ~3.5 Ga is not well established, but was likely less than 150 °C (Ganne and Feng, 2017, Aulbach and Arndt, 2019). Using the experimental oxybarometer of Ballhaus et al. (1991), we estimated the change in oxygen fugacity that would be caused by decrease in the mantle potential temperature by 150 °C, from 1800 °C to 1650 °C, assuming a constant pressure of 2.0 GPa, and constant X^{spinel}_{Fe+3} of 0.05, X^{spinel}_{Fe+2} of 0.55, X^{spinel}_{Al} of 0.4, and $X^{olivine}_{Fe}$ of 0.1. Our calculations indicate that this decrease in temperature would be equal to an increase of 0.02 ΔFMQ log units in oxygen fugacity, which is smaller than the uncertainty on the fO_2 estimates for all the magmatic systems in this study. We conclude, therefore, that secular change in the mantle potential temperature had no measurable effect on the calculated oxygen fugacities for the studied systems, and that the trend observed in Fig. 5a is not the result of mantle cooling, nor was the trend significantly dispersed by it.

5.2.3. The effects of depth of mantle melting and upwelling on fO_2

Another issue to address is the difference in the depth of melt segregation for the studied systems and its effect on the calculated fO_2. It has been argued that the oxygen fugacity of the mantle decreases with increasing depth due to pressure dependence of the garnet-fayalite-ferrosilite-O_2 equilibrium (Woodland and Koch, 2003). However, this calibration is only relevant until the depth of metal saturation, beyond which fO_2 shows comparatively little pressure dependence (Frost et al., 2008). Although melting in the studied plume lavas took place at depths that are not well constrained, there is no evidence that melts segregated at greater depths in older samples than in their younger counterparts. The Kilauea Iki lavas yielded fO_2 that is among the highest of the measured values, but were derived from melting well into the garnet stability field (Norman and Garcia, 1999), opposite to the predicted trend of Woodland and Koch (2003). In addition, the relationship between the depth of melting initiation and fO_2 is not straightforward due to the fact that the melts likely remained in equilibrium with the mantle residue well past the depth of melt initiation. The Al_2O_3/TiO_2 ratio has been shown to vary with depth of segregation of a komatiitic melt from its mantle residue (Nesbitt and Sun, 1976; Sossi et al., 2016), but there is no correlation between fO_2 and average Al_2O_3/TiO_2 ratio evident in our data.

The FMQ redox buffer follows the redox evolution of a decompressing melt within ~0.17 log units/GPa (Kress and Carmichael, 1991), so that oxygen fugacity values expressed in ΔFMQ terms largely retain their validity through decompression melting (Kelley and Cottrell, 2012). This difference is small enough that it is within uncertainty of most of the fO_2 determinations. This is one of the reasons that fO_2 of volcanic rocks relative to the FMQ buffer has been previously used as a reference point for determining upper mantle oxygen fugacity (e.g., Kelley and Cottrell, 2012). Finally, the obtained redox data for the studied systems were compared to the fO_2 of modern-day MORB and plume lavas, as opposed to modern peridotites, in an attempt to minimize the differential effects of decompression on the calculated oxygen fugacities. We, therefore, conclude that differences in depth of melting are likely not the cause for the secular trend in oxygen fugacity observed in Fig. 5a.

5.2.4. The effects of magma degassing and differentiation on fO_2

Two additional factors that have been shown to have an effect on the oxygen fugacity of an evolving magma are fractional crystallization and volatile degassing. Olivine fractionation removes Fe^{2+} and, thus, changes the oxygen fugacity of mafic magmas evolving as closed systems (Cottrell and Kelley, 2011; Sossi et al., 2012). However, this effect is relatively minor for the magmas studied here, which experienced little differentiation prior to emplacement, as their high MgO contents show that they are close to composition of primary mantle melts. Moreover, the Winnipegosis and Song Da komatiite suites and the Onega Plateau picrites all have fO_2 values within error of each other but range in their emplaced lava MgO content from 7.95 $\pm$ 0.28 to 21.1 $\pm$ 2.5 wt.%. Theory predicts that lower-MgO lavas should exhibit higher fO_2, but the Padloping Island lavas are the most reduced lavas measured in this study, despite the fact that they are less MgO-rich than most of the others (Tables 5 and 6). We, thus, conclude that olivine fractionation had a negligible effect on the measured fO_2 values of the lavas.

Degassing of sulfur has been shown to have a strong control on the fO_2 of an evolving picritic (Moussallam et al., 2016) or phonolitic (Moussallam et al., 2014) magma.

Sulfur is largely present as S^{2-} in mantle-derived magmas, which can be degassed as SO_2 according to the following equation from Métrich et al. (2009):

$$S^{2-} + 4Fe_2O_3 \rightarrow S^{6+}O_2 + 8FeO + 2O^{2-} \quad (2)$$

Eq. (2) shows that for each mole of sulfur degassed as SO_2, 8 moles of Fe^{3+} are reduced to Fe^{2+}. It has been demonstrated for Kilauea Iki lava lake that sulfur degassing had a resolvable reducing effect on the evolving magma, and the un-degassed picritic magma was estimated to have had an oxygen fugacity of $\sim\Delta NNO = 0$ (Moussallam et al., 2016). Our value of $\Delta NNO = +0.80 \pm 0.27$ for Kilauea Iki is higher than this estimate, and may reflect rapid quenching of the uppermost section of the lava lake prior to extensive degassing, or alternatively, may reflect inter-calibration issues between the V partitioning and $Fe^{3+}/\Sigma Fe$ ratio oxybarometers.

The highly siderophile element abundance data indicate that the Schapenburg lavas were sulfide undersaturated (Puchtel et al., 2016a), and, thus, likely degassed little sulfur. Chalcophile elements, such as Cu, Pd and Pt, behaved incompatibly during differentiation of Gorgona komatiites (Brügmann et al., 1987), and this suite was, therefore, also sulfur-undersaturated. Although sulfide saturation depletes an evolving melt in sulfur, high-degree melts that never experienced sulfide saturation, like those studied here, did not experience sulfide saturation because they contained very low concentrations of sulfur. Sulfide undersaturation therefore requires the lack of significant sulfur degassing in the studied ultramafic rocks. Sulfur degassing in the Lapland and Onega Plateau systems was also likely relatively minor due to their subvolcanic nature. It is also worth noting that the Gorgona, Schapenburg and Winnipegosis komatiites erupted sub-aqueously, which likely minimized sulfur degassing. It is unknown what effect sulfur degassing had on the measured fO_2 of the Song Da komatiites and the Iceland and Padloping Island picrites. Unless initial conditions were extremely oxidizing, such as those found in arc basalts, degassing of sulfur has only been shown to cause reduction and not oxidation (Moussallam et al., 2014, 2016; Brounce et al., 2017), and, thus, the fO_2 values for these systems likely represent the minimum values. There is no *a priori* reason why the older systems would have degassed more sulfur than the younger systems, and, therefore, the observed trend of secular oxidation is likely not caused by variable amounts of sulfur degassing. We, thus, conclude that the secular oxidation trend observed in our data likely represents oxidation of the mantle source regions of these lavas with time.

5.3. Mechanisms for oxidation of the mantle

Our data indicate an increase of 1.33 ± 0.43 ΔFMQ log units over 1.6 Ga of Earth history, which is within uncertainties of the 0.93 ± 0.55 ΔFMQ log unit difference between Archean and modern samples estimated by Aulbach and Stagno (2016) using the V/Sc oxybarometer. The conclusion that the Earth's mantle has oxidized since the Archean is also supported by the study of Aulbach et al. (2017a), which used $Fe^{3+}/\Sigma Fe$ ratios in eclogitic garnets to determine that subducted Archean oceanic crust was likely more reduced than the present-day oceanic crust. Additionally, Foley (2011) suggested that the lack of carbonatites in the geologic record prior to 2.7 Ga was the result of the mantle at that time being more reduced than the present-day mantle. Compared to our data, the Aulbach and Stagno (2016) dataset shows significantly lower absolute oxygen fugacity values in both Archean picrites and modern MORB. This is likely due to issues with inter-calibration of different oxybarometers, as discussed by Mallmann and O'Neill (2013), or due to differences in mantle melting processes between ridge and plume settings. Despite this, the agreement between the magnitude of our trend and the Aulbach and Stagno (2016) trend is remarkable, and offers further support to the notion that the mantle has experienced significant secular oxidation. In the following sections, we discuss the mechanisms that might have been responsible for the observed change in the redox state of the mantle.

An increase in the oxygen fugacity of the mantle of ca. 1.3 ΔFMQ log units is a significant change for a reservoir as large as the mantle, which comprises ~84% of the Earth's volume and ~68% of the Earth's mass. Changing the mantle's redox state by 1.3 ΔFMQ log units would require the addition of a large and likely geochemically detectable amount of oxidized material. Three possible scenarios are considered as potential mechanisms for oxidizing the mantle: (1) recycling of oceanic crust, (2) venting of oxygen from the core, and (3) homogenization of early formed mantle heterogeneities. None of these mechanisms are mutually exclusive, and all may have contributed to the observed trend.

5.3.1. *Recycling of oceanic crust*

The most obvious explanation for an increase in the oxygen fugacity of the mantle comes from evaluating the effects of modern plate tectonic processes. Oceanic crust returning into the mantle at subduction zones is more oxidized than the crust emerging at spreading centers as a result of interaction with O_2 and H_2O on the Earth's surface. Serpentinization reactions reduce seawater to generate H_2 gas, which may subsequently be lost to space. The low molecular mass of the H_2 gas makes it one of the few volatile species to readily escape from the Earth's atmosphere, acting as a net oxidant to the entire Earth system (Catling et al., 2001). However, H_2 gas produced in an oxygenated atmosphere rapidly reacts with O_2 and, therefore, remains in the Earth system (Zahnle et al., 2013). As a consequence of serpentinization, Fe^{2+} in altered oceanic crust (AOC) is oxidized to Fe^{3+} to form magnetite, enriching the AOC package in Fe^{3+}. For example, serpentinites have $Fe^{3+}/\Sigma Fe$ of ~0.3 (Padron-Navarta et al., 2011), greatly in excess of the mantle value of 0.02–0.05 (Cottrell and Kelley, 2011). However, the amount of oxidized material that makes it into the deep mantle remains largely unknown. Some of that oxidized material is likely lost to generate the oxidized mantle wedge and the comparatively oxidized arc lavas (Parkinson and Arculus, 1999; Brounce et al., 2014).

Mass balance calculations indicate that subduction is a net oxidant for the mantle even today, after accounting

for the oxidants lost in arc lavas and gases and those brought back up by MORB and OIB volcanism (Evans, 2012). The mass balance of various fluxes indicates that Fe^{3+} is the main oxidant making it through subduction zones to the deep mantle, while SO_4^{2-} and CO_3^{2-} are largely returned to the surface in arc volcanoes (Evans, 2012). The net oxidation flux for the modern Earth's mantle is estimated at $46 \pm 12 \times 10^{12}$ mol/yr (Evans, 2012), similar to the earlier estimates (7.1×10^{12} moles of oxidant/year) which only took into account Fe^{3+} flux and also relied on an older understanding of serpentinization reactions (Lécuyer and Ricard, 1999).

Using the mantle oxidation equations of Evans (2012), and their estimated present-day subduction flux of oxidants, we tested the hypothesis of whether crustal recycling is a viable mechanism for mantle oxidation. Starting with the oxidation state of the Komati system of -0.11 ± 0.30 ΔFMQ log units at 3.48 Ga, we allow the mantle to mix in crust at present day rates up to 1.87 Ga, when the oxidation trend flattened out. Our calculations show that the mantle would have only been oxidized from −0.11 to +0.38 ΔFMQ log units over the ~1.6 Ga period, i.e., an increase in the redox state of the mantle of ~0.49 ΔFMQ log units, which falls short of the oxygen fugacity of the Winnipegosis komatiites by ~0.71 ΔFMQ log units.

For the sake of the modeling, we varied the subduction redox flux and the fraction of the mantle participating in the mixing. Increasing the subduction redox flux by a factor of ~4 results in a mantle oxidation of +1.22 ΔFMQ log units by 1.87 Ga, which is consistent with the oxidation state of the Winnipegosis komatiites. Reducing the fraction of the mantle participating in the mixing calculation to ~25% of the mantle's total mass achieves the same effect. One of the major weaknesses of this model is that there is no *a priori* reason why oxidation of the mantle would cease in the Paleoproterozoic, as oxidized slab material likely continued to be recycled into the mantle well past 1.87 Ga. Another weakness of this model is that with little agreement on the existence of modern-style plate tectonics in the Archean, there are no strong constraints on the crustal recycling rate during that period. The question of whether modern-style mobile-lid plate tectonics operated during the Archean has been the subject of much debate (e.g., Sizova et al., 2010; Moore and Webb, 2013; Gerya, 2014), but some mode of crustal recycling must have existed during the Archean, and any such tectonic process could theoretically bring oxidized material back into the mantle. The altered oceanic crust in the early Earth was also likely less oxidized than the present day crust until ~800 Ma (Stolper and Keller, 2018). The results of our modeling represent an upper limit on the amount of oxidation resulting from this mechanism, given the few constraints on the oxidation state of Archean altered oceanic crust and the possibly lower rates of crustal recycling in the Archean. It appears unlikely that the subduction redox flux at any time in Earth history was ~4 times greater than that of the present day and equally unlikely that ~75% of the mantle did not participate in convective mixing.

Based on all the arguments presented above, we conclude that the crustal recycling model is unlikely to account for the change in the redox state of the mantle of ~1.3 ΔFMQ log units required by the data. However, further work to quantify Precambrian crustal recycling rates and the oxidation state of deeply subducted slabs may affect this conclusion.

5.3.2. Venting of oxygen from the core

The second possible mechanism of progressive oxidation of the mantle involves venting of oxygen from the outer core into the lower mantle. The Earth's core contains substantial amounts of light elements, such as Si, S, and O (e.g., Birch, 1964; Badro et al., 2015). Initially, Earth's core is thought to have been entirely molten and, as the Earth cooled, the inner core began to crystallize and grew over time. It has been shown experimentally (Badro et al., 2007), through modeling (Badro et al., 2015), and via ab initio calculations (Alfè et al., 2002) that the solid metal of the inner core would preferentially exclude O, but would incorporate significant amounts of Si and S. Crystallization of the inner core, thus, enriches the outer core in dissolved O and, if the outer core were to become supersaturated with respect to O, some of this oxygen could have escaped into the lower mantle. This model removes the problems associated with the large amounts of recycled material required to oxidize the mantle, because the mass of the outer core is similar in magnitude to the mass of the mantle. Using the present-day size of the inner core and the O concentration estimates of Alfè et al. (2002), the amount of oxygen added to the outer core from inner core crystallization is calculated to be $\sim 10^{24}$ moles. This is ~0.25 moles oxygen/kg of the mantle mass, far more than is needed to oxidize the relatively reduced mantle by ~1.3 log units. However, this upper limit of oxygen released into the mantle does not take into account gradual inner core growth, and assumes that all of the oxygen released as the result of inner core crystallization is transferred to the mantle. Neither of these are safe assumptions. The maximum amount of oxygen that can be dissolved in the outer core is not experimentally constrained and likely varies with outer core temperature. It is also unknown whether a supersaturated outer core would lose molecular O_2 (a mantle oxidant) or FeO (a mantle reductant). Existing constraints indicate that FeO is the likely phase that would exsolve from an outer core supersaturated in oxygen (Humayun et al., 2004), making this mechanism invalid. However, additional high-pressure experimental data are necessary. In addition, the existence of chemical exchange between the core and mantle is still debated, based mostly on the available isotopic data for plume-derived lavas (Brandon et al., 1999, 2003; Baker and Jensen, 2004; Brandon and Walker, 2005; Puchtel et al., 2005; Luguet et al., 2008; Ireland et al., 2011).

Perhaps the most central issue with this model is the fact that the timing of the onset of inner core crystallization is poorly constrained (e.g., Buffett, 2003). The overall oxidation trend revealed by the data from this study begins at 3.5 Ga and continues to 1.87 Ga, necessitating early inner core formation for outer core O saturation to be the driving mechanism behind the observed mantle oxidation trend. Models of core-mantle interaction based on geochemical

evidence of leakage of Os from the outer core into the lower mantle require an early onset of inner core crystallization, ranging from 3.0 to 4.2 Ga (Brandon et al., 2003; Puchtel et al., 2005). In contrast, thermal history models favor a younger age for the inner core, e.g., ca. 1.0 $Ga^{1.0+}_{-1.5}$ (Labrosse et al., 2001). The presence of significant concentrations of radioactive elements in the core (e.g., K), or the existence of a radioactive element-enriched "slab graveyard" at the core-mantle boundary could push the onset of inner core crystallization back to 3.0 Ga. Overall, there is little agreement among researchers on the timing of the onset of inner core crystallization; as such, the mechanism presented here remains largely speculative. Recent geochemical evidence for relatively sluggish mixing of the mantle (e.g., Touboul et al., 2012; Rizo et al., 2016; Puchtel et al., 2016a; Mundl et al., 2017) also contradicts this model. Oxygen leaving the outer core would escape into the lower mantle upward in all directions, and the upper and lower mantle need to be efficiently mixed in order to facilitate mantle oxidation.

As a further issue to account for in models of core-mantle interaction, any large-scale chemical exchange between the core and mantle would likely result in large enrichments in the highly siderophile elements (HSE), coupled enrichments in $^{186,187}Os$ (Brandon et al., 1999, 2003; Ireland et al., 2011), and strongly negative $\mu^{182}W$ isotopic anomalies (Touboul et al., 2012) in plume-derived lavas that originated at the core-mantle boundary. However, large HSE enrichments have not been observed in the mantle sources of any of the magmatic systems studied here.

Tungsten isotopic anomalies have only been detected in the Kilauea Iki, Padloping Island and Schapenburg systems (Rizo et al., 2016; Mundl et al., 2017; Puchtel et al., 2016a). Mundl et al. (2017) concluded, however, that the negative $\mu^{182}W$ signal in the Kilauea Iki lave lake is unlikely to originate from the outer core. The source region of the Schapenburg komatiite system with a negative $\mu^{182}W$ anomaly is strongly depleted in the HSE relative to BSE and, thus, likely experienced no core-mantle exchange (Puchtel et al., 2016a), while the Padloping Island's positive $\mu^{182}W$ signal is opposite to what would be expected from addition of outer core material. The Schapenburg and Padloping Island systems were also excluded from the ISOPLOT regression calculations illustrated in Fig. 5a. There is, thus, no strong evidence, isotopic or otherwise, for addition of core material to the mantle source regions of any of the studied systems, although it is possible that a light element, such as O, could vent to the mantle without entraining any other elements. Overall, better constraints on the maximum O content of the outer core, the timing of the onset of the inner core crystallization, and the mechanisms of core-mantle interaction are necessary to further determine the viability of this model.

5.3.3. Mixing of primordial mantle redox heterogeneities

According to the commonly accepted scenario of early Earth evolution, the silicate Earth melted and differentiated early in its history due to the energetic impacts associated with planetary accretion, and the release of heat associated with core formation (Matsui and Abe, 1986; Tonks and Melosh, 1993). This early differentiation facilitated the fractionation of short-lived isotope systems, isotopic anomalies of which are found in Precambrian and even in modern rocks (Touboul et al., 2012; Willbold et al., 2015; Rizo et al., 2016; Puchtel et al., 2016a, Mundl et al., 2017).

In order to segregate a core made of Fe-Ni alloy, the primordial mantle must have been reducing enough to be in equilibrium with metallic Fe, i.e., its redox state must have been close to the iron-wüstite (IW) buffer. The five orders of magnitude higher oxidation state of the present-day mantle than the IW buffer has been proposed to be the result of Fe (II) disproportionation reactions in the deep mantle and loss of Fe metal to the core in down-going metallic diapirs (Wood et al., 2006; Frost and McCammon, 2008). In this model, Fe^{2+} disproportionates to Fe^{3+} and Fe metal at high pressures in the lower mantle, which enables Fe^{3+} to enter the predominant bridgmanite crystal structure at these depths. Some of this disproportionated Fe metal was subsequently lost to the core, leaving a more oxidized lower mantle that was no longer in redox equilibrium with the core. The early terrestrial mantle would thus consist of a relatively reduced upper mantle sitting atop a relatively oxidized lower mantle. This model is supported by the observation that the lunar mantle is highly reduced due to the fact that the pressures at the bottom of the lunar magma ocean were not high enough to stabilize bridgmanite (Frost et al., 2008).

The komatiite and picrite systems studied here may represent relatively deep mantle melts, but constraining the depth at which the respective mantle plumes that gave rise to these systems originated is difficult. Assuming all the systems were representative of the upper mantle in terms of their redox state at the time of their formation, then the upper mantle has presumably mixed with a more oxidized lower mantle to produce oxidation with time. It is unclear whether this process was continuous or episodic. As there is no mantle oxidation observed after 1.87 Ga, it is possible that the main homogenization event had already occurred by 1.87 Ga, possibly due to the initiation of mobile-lid plate tectonics at the Archean-Proterozoic boundary, which efficiently mixed away much, but not all, of the early-formed mantle isotopic heterogeneities (Debaill et al., 2013; Mundl et al., 2017). Since the heterogeneities produced by the ^{182}Hf-^{182}W isotope system persist to the present day, it is, thus, not unreasonable to suggest that early redox heterogeneities may have persisted well into the Paleoproterozoic. It is likely that the mantle has become more homogenous with time due to convective stirring, which makes progressive mixing between the upper and lower mantle a viable mechanism for explaining upper mantle oxidation.

A supporting argument for this mechanism is provided by the high fO_2 of the Schapenburg komatiite system relative to komatiite systems of similar age within the same craton, such as the 3.48 Komati and 3.26 Weltevreden systems (Nicklas et al., 2018). Isotopic constraints from both short- and long-lived isotope systems indicate that the mantle source region of the Schapenburg komatiites fractionated bridgmanite within the first ~30 Ma of solar system formation (Puchtel et al., 2016a). No such short-lived anomalies

have been found in the source region of the other Kaapvaal Craton komatiites studied (Touboul et al., 2012; Puchtel et al., 2013, 2014). Thus, the Schapenburg source region was formed in the lower mantle close to the time of core formation and was preserved until 3.55 Ga. The high oxidation state of the Schapenburg system likely reflects the loss of disproportionated Fe metal in its source region during an early magma ocean stage. Mixing between a theoretical "Schapenburg-type" mantle with high fO_2 and a "Komati-type" mantle with the low fO_2 could have resulted in the observed trend. Although the Schapenburg system is not as oxidized as some of the Phanerozoic systems, the "Schapenburg-type" endmember may have extended to higher fO_2 than observed in the Schapenburg komatiites. This mantle oxidation scenario has been previously advocated by Nicklas and Puchtel (2016), Aulbach and Stagno (2016) and Andrault et al. (2018). However, more investigation into the oxidation state of ultramafic rocks showing short-lived isotope anomalies, and into the thermodynamics of mixing mantle regions of different oxidation states, are needed to further constrain this model.

5.4. The Schapenburg and Padloping Island Systems and Early Earth Redox

As mentioned in the previous sections, both the Schapenburg komatiite and Padloping Island picrite systems show resolved anomalies in the short-lived ^{182}Hf-^{182}W isotope system. In addition to a negative ^{182}W anomaly, the Schapenburg komatiite system has a negative ^{142}Nd anomaly, as well as decoupled long-lived ^{176}Lu–^{176}Hf and ^{147}Sm–^{143}Nd systems, indicating fractionation of the lower mantle phases bridgmanite and Ca-perovskite very early in its mantle source region's history (Puchtel et al., 2016a). The Padloping Island picrites have the largest known terrestrial ^{182}W anomaly (Rizo et al., 2016), but do not show any resolvable anomaly in ^{142}Nd (De Leeuw et al., 2017). The lack of a ^{142}Nd anomaly rules out crystal-liquid silicate fractionation as a mechanism for generating the large ^{182}W anomalies in the Padloping Island picrites. Early metal-silicate fractionation could have produced large ^{182}W anomalies with no effect on the lithophile Sm-Nd isotope system, indicating that this is the likely mechanism for generating the source region of the Padloping Island lavas (Rizo et al., 2016).

Although both the Padloping Island and Schapenburg komatiite systems have short-lived isotope anomalies and are excluded from the regression of the fO_2 data in Fig. 5a, the Schapenburg komatiites are characterized by a higher oxidation state relative to systems of the same age, while the Padloping Island lavas are within uncertainties of most other plume-derived Phanerozoic lavas, and also overlap with the range of modern MORB in terms of their fO_2. The Schapenburg source likely lost disproportionated Fe to the core early in its history, leading to the high oxidation state of Schapenburg lavas. There is no evidence for the Padloping source region being in the bridgmanite stability field during core-forming events, and thus it is not expected to show an elevated fO_2 value. Indeed, the equilibration of the Padloping Island source region with metal (Rizo et al., 2016) likely greatly lowered its fO_2, but this signature was possibly later diluted by ambient mantle to create a mantle region with large ^{182}W anomalies but only slightly lower fO_2 than the source regions of other plume lavas of the same age. These two magmatic systems illustrate that relationships between oxidation state and short-lived isotope anomalies in plume-derived lavas may not be straightforward.

5.5. Relationship between mantle oxidation state and atmospheric O_2 content

The Great Oxidation Event (GOE) marked one of the most dramatic changes in the Earth's surficial environment. Molecular oxygen rose from trace levels in the Archean atmosphere ($<10^{-6}$ atm) to become a small but significant constituent of the atmosphere in the Proterozoic, eventually rising to ~0.2 atm in the Phanerozoic. The exact timing and tempo of the GOE are complex, but it is denoted most clearly in the geochemistry of sulfur isotopes (Farquhar et al., 2000). Specifically, the disappearance of mass independent sulfur isotope fractionation (Δ^{33}S) in sedimentary rocks, beginning between 2.461 and 2.308 Ga (Gumsley et al., 2017), is best-explained by the accumulation of sufficient atmospheric O_2 to oxidize and homogenize isotopically fractionated atmospheric S reservoirs produced by UV-driven photochemistry (Ono, 2017).

The exact causes of the GOE remain unclear. Oxidative photosynthesis is the source of O_2 to the atmosphere, but also of organic carbon. In biological respiration, O_2 reacts with organic carbon, removing O_2 from the atmosphere. In fact, on an annual basis, O_2-producing photosynthesis and O_2-consuming respiration are in almost perfect equilibrium (Catling, 2014). Therefore, accumulation of O_2 in the atmosphere requires: (a) photosynthetic production of O_2; (b) burial of photosynthetically produced organic carbon for geologically significant periods of time, leaving behind unrespired O_2 in the surface environment; (c) that this net biogeochemical process produces O_2 at rates sufficient to overwhelm geological sinks of O_2, such as the oxidation of Fe^{2+} and other reductants in crustal rocks and hydrothermal systems, and the oxidation of reduced gases derived from the mantle.

It is likely that a decrease in the strength of geological sinks was a critical contributor to the GOE. Two lines of evidence are particularly important. First, although it is tempting to conclude that the GOE was caused by the proximal emergence of oxygenic photosynthesis (Fischer et al., 2016), multiple lines of geochemical and genomic evidence are consistent with biological O_2 production originating well before 2.4 Ga (e.g., Lyons et al., 2014), and arguably as early as ~3.0 Ga (Planavsky et al., 2014). Hence, it is highly unlikely that the GOE is a direct and simple consequence of biological evolution.

Second, the carbon isotope record in sedimentary rocks can be used to place constraints on the extent of burial of organic carbon through time (Schidlowski, 1988), and, hence, on whether there could have been a change in net biogeochemical production of O_2. A recent statistical re-examination of this record revealed that the fraction of

carbon leaving the surface environment as organic carbon ("f_{org}") did, indeed, increase steadily through the Precambrian (Krissansen-Totton et al., 2015). However, the extent of this increase does not appear to be sufficient to account for the O_2 accumulation represented by the GOE (Krissansen-Totton et al., 2015).

Attention, therefore, turns to the extent of O_2 consumed by geological sinks. Reactions with volcanic gases, such as CO, H_2S and H_2, are major sinks for atmospheric O_2. The reducing capacity of volcanic gases is controlled by their fO_2, which is, in turn, largely buffered by the fO_2 of the degassing lava during cooling (Gerlach, 1993; Kasting et al., 1993), making igneous and, therefore, mantle fO_2 an important factor in atmospheric evolution.

Although the relationship between mantle fO_2 and volcanic gas fO_2 is complicated by many factors, such as degassing pressures (e.g., Gaillard et al., 2011), it has been shown that an increase of ~0.50 log units in the oxidation state of the mantle sources of volcanoes between the Archean and Proterozoic could have reduced the volcanic gas O_2 sink to explain the GOE (Holland, 2002). This hypothesized shift is well within the range indicated by our data. Therefore, the data presented here suggest that the oxidation state of the atmosphere is most likely coupled to that of the deep Earth, with important implications for the GOE.

The idea that the GOE was triggered by homogenization of the mantle with an oxidized lower mantle component has been previously advocated (Nicklas and Puchtel, 2016; Aulbach and Stagno, 2016; Andrault et al., 2018), and this scenario is consistent with our data. We do not necessarily argue that the progressive mantle oxidation over time was the sole trigger of the GOE, as other important factors that affected geological O_2 sinks may have played a role, including the growth of felsic continents (Lee et al., 2016), the rise of subaerial volcanism (Kump and Barley, 2007), or large flood basalt events (Ciborowski and Kerr, 2016).

6. CONCLUSIONS

Oxygen fugacity has been studied in nine komatiite and picrite systems ranging in age from 3.55 Ga to the present day using V partitioning between liquidus olivine and host lavas. These systems were considered together with the six komatiite systems previously studied by Nicklas et al. (2016; 2018). The systems dated from 3.48 Ga to 1.87 Ga define a secular trend of increasing oxygen fugacity of the mantle from -0.11 ± 0.30 to $+1.22 \pm 0.31$ ΔFMQ log units, a change of 1.33 ± 0.43 ΔFMQ log units over 1.61 Ga of Earth's history. Several mechanisms for oxidation of the mantle are considered, including recycling oceanic crust, venting O from the outer core, and mixing in of primordial mantle redox heterogeneities.

Our modeling indicates that subducted redox fluxes ~4 times that of the present-day Earth are required to achieve the change in oxidation state observed in our data. Alternatively, having only <25% of the mantle participating in mixing with subducted slabs achieves the same effect. Both of these scenarios seem unlikely given the anoxic oceanic conditions in the Archean and the likely lack of modern-style plate tectonics during the same period.

Inner core crystallization is theoretically capable of delivering orders of magnitude more oxygen than that required to oxidize the mantle to the degree established in this study, provided that the outer core became supersaturated with respect to O and vented O into the lower mantle without causing collateral entrainment of any other geochemically detectable outer core material. The viability of this mechanism is contingent upon the early onset of inner core crystallization and the low solubility of O in the outer core, both of which are presently poorly constrained.

The iron disproportionation model of primordial mantle oxidation (Frost et al., 2008) requires that the lower mantle (bridgmanite stability field) became more oxidized than the upper mantle immediately following core formation. The observation that the source region of 3.55 Ga Schapenburg komatiites was in the bridgmanite stability field early in Earth history and was isolated from the convecting mantle until the time of komatiite formation, and the fact that the system shows relatively high fO_2 indicate that lower mantle-derived primordial redox heterogeneities persisted well into the Archean. Mixing in of "Schapenburg-type" mantle with the accessible convecting mantle is a possible mantle oxidation mechanism. Additional data on the oxidation state of the early lower mantle and mantle mixing rates during the Archean are needed to better constrain this model, but we consider it the most plausible of the three mechanisms discussed here.

Due to difficulties with comparing the results of different oxybarometers, additional work using the V-partitioning oxybarometer is needed for well documented mantle-derived rocks of all ages in order to further constrain the redox evolution of the mantle. Most notably, only four MORB samples have been studied using this method and future work should focus on increasing the amount of available MORB data.

The temporal trend in mantle fO_2 documented in this study most likely points to the involvement of deep mantle oxidation in the surficial oxidation seen during the GOE. Although more modeling is necessary to clarify the relationship between the change in the oxidation state of the mantle and the GOE, it is evident that the mantle played an important role in this fundamental change in Earth's surficial environment.

ACKNOWLEDGEMENTS

This study was supported by NSF FESD Type I Grant #1338810 "The Dynamics of Earth System Oxygenation" (lead PI is A.D. Anbar, I.S. Puchtel is a co-PI). This source of support is gratefully acknowledged. Eero Hanski acknowledges support from Academy of Finland Grant #281859. The authors wish to thank Nadezhda Tolstykh and Andrey Vishnevsky for providing the Song Da samples VS 5-1, VS 6-1 and VS 6-2, and Alan Brandon for providing the Icelandic samples ICE4A, ICE4B, and ICE5. We thank Valentina Puchtel for help with sample preparation. We also thank Mark Fornace (undergraduate assistant), Valentina Puchtel, and William F. McDonough for their assistance in the initial development of the standard addition technique, which was supported by NSF grant EAR-0739006 (to W.F.M.). The support of the Maryland NanoCenter and its AIMLab is gratefully acknowledged. Finally, thorough reviews by Dr. Sonja Aulbach and Dr. Guilherme Mallmann, as well as comments by Associate

Editor Dr. Munir Humayun, greatly improved the initial version of this manuscript.

APPENDIX A. SUPPLEMENTARY MATERIAL

Supplementary data to this article can be found online at https://doi.org/10.1016/j.gca.2019.01.037.

REFERENCES

Alfè D., Gillan M. and Price G. (2002) Composition and temperature of the Earth's core constrained by combining ab initio calculations and seismic data. *Earth Planet. Sci. Lett.* **195**, 91–98.

Andrault D., Muñoz M., Pesce G., Cerantola V., Chumakov A., Kantor I., Pascarelli S., Ruffer R. and Hennet L. (2018) Large oxygen excess in the primitive mantle could be the source of the Great Oxygenation Event. *Geochem. Persp. Lett.* **6**, 5–10. https://doi.org/10.7185/geochemlet.1801.

Anh T. V., Pang K. N., Chung S. L., Lin H. M., Hoa T. T., Anh T. T. and Yang H. J. (2011) The Song Da Magmatic Suite revisited: a petrologic, geochemical and Sr-Nd isotopic study of picrites, flood basalts and silicic volcanic rocks. *J. Asian Earth Sci.* **42**, 1341–1355.

Anhaeusser C. R. (1983) The geology of the Schapenburg greenstone remnant and surrounding Archaean granitic terrane south of Badplaas, Eastern Transvaal. *Geol. Soc. S. Afr Spec. Publ.* **9**, 31–44.

Anhaeusser C. R. (1991) Schapenburg greenstone remnant. In *Two Cratons and an Orogen—Excursion Guidebook and Review Articles for a Field Workshop Through Selected Archaean Terranes of Swaziland, South Africa and Zimbabwe* (ed. L. D. Ashwal). Univ. of the Witwatersrand, Johannesburg, South Africa, pp. 107–115.

Anhaeusser C. R. and Robb L. J. (1980) Regional and detailed field and geochemical studies of Archaean trondhjemitic gneisses, migmatites and greenstone xenoliths in the southern part of the Barberton Mountain Land, South Africa. *Precambrian Res.* **11**, 373–397.

Arndt N. T. (1986a) Spinifex and swirling olivines in a komatiite lava lake, Munro Township, Canada. *Precambrian Res.* **34**, 139–155.

Arndt N. T. (1986b) Differentiation of komatiite flows. *J. Petrol.* **27**, 279–301.

Aulbach S. and Arndt N. T. (2019) Eclogites as paleodynamic archives: evidence for warm (not hot) and depleted (but heterogeneous) Archean ambient mantle. *Earth Planet. Sci. Lett.* **505**, 162–172.

Aulbach S., Woodland A. B., Vasilyev P., Galvez M. E. and Viljoen K. S. (2017a) Effects of low-pressure igneous processes and subduction of $Fe^{+3}/\Sigma Fe$ and redox state of mantle eclogites from Lace (Kaapvaal Craton). *Earth Planet. Sci. Lett.* **474**, 283–295.

Aulbach S., Sun J., Tappe S., Hofer H. and Gerdes A. (2017b) Volatile-rich metasomatism in the cratonic mantle beneath SW Greenland: link to kimberlites and mid-lithospheric discontinuites. *J. Petrol.* **58**, 2311–2338.

Aulbach S. and Stagno V. (2016) Evidence for a reducing Archean ambient mantle and its effects on the carbon cycle. *Geology* **44**, 751–754.

Aulbach S. and Viljoen K. S. (2015) Eclogite xenoliths from the Lace kimberlite, Kaapvaal craton: from convecting mantle source to palaeo-ocean floor and back. *Earth Planet. Sci. Lett.* **431**, 274–286.

Badro J., Fiquet G., Guyot F., Gregoryanz E., Occelli F., Antonangeli D. and D'astuto M. (2007) Effect of light elements on the sound velocities in solid iron: implications for the composition of Earth's core. *Earth Planet. Sci. Lett.* **254**, 233–238.

Badro J., Brodholt J. P., Piet H., Siebert J. and Ryerson F. J. (2015) Core formation and core composition from coupled geochemical and geophysical constraints. *Proc. Natl. Acad. Sci. USA* **112**, 12310–12314.

Baker J. A. and Jensen J. K. (2004) ^{186}Os-^{187}Os enrichments in the Earth's mantle: core-mantle interaction or recycling of ferro-manganese crusts and nodules? *Earth Planet Sci. Lett.* **220**, 277–286.

Ballhaus C., Berry R. F. and Green D. H. (1991) High pressure experimental calibration of the olivine-orthopyroxene-spinel oxygen geobarometer: implications for the oxidation state of the upper mantle. *Contrib. Mineral. Petrol.* **107**, 27–40.

Barnes S. J., Hill R. E. T. and Gole M. J. (1988) The Perseverance ultramafic complex, Western Australia: the product of a komatiite lava river. *J. Petrol.* **29**, 305–331.

Baragar W. R. A. and Scoates R. F. J. (1981) The circum-superior belt: a proterozoic plate margin? In *Precambrian Plate Tectonics* (ed. A. Kröner). Elsevier, Amsterdam, pp. 297–330.

Beattie P., Ford C. and Russell D. (1991) Partition coefficients for olivine-melt and orthopyroxene-melt systems. *Contrib. Mineral. Petrol.* **109**, 212–224.

Berry A. J., Danyushevsky L. V., O'Neill H., St C., Newville M. and Sutton S. R. (2008) Oxidation state of iron in komatiitic melt inclusions indicates hot Archaean mantle. *Nature* **455**, 960–963.

Birch F. (1964) Density and composition of mantle and core. *J. Geophys. Res.* **69**, 4377–4388.

Blichert-Toft J., Arndt N. T. and Gruau G. (2004) Hf isotopic measurements on Barberton komatiites: effects of incomplete sample dissolution and importance for primary and secondary magmatic signatures. *Chem. Geol.* **207**, 261–275.

Bottinga Y. and Javoy M. (1990) MORB degassing: bubble growth and ascent. *Chem. Geol.* **81**, 255–270.

Brandon A. D., Graham D. W., Waight T. and Gautason B. (2007) ^{186}Os and ^{187}Os enrichments and high-$^{3}He/^{4}He$ sources in the Earth's mantle: evidence from Icelandic picrites. *Geochim. Cosmochim. Acta* **71**, 4570–4591.

Brandon A. D. and Walker R. J. (2005) The debate over core-mantle interaction. *Earth Planet. Sci. Lett.* **232**, 211–225.

Brandon A. D., Walker R. J., Puchtel I. S., Becker H., Humayun M. and Revillon S. (2003) ^{186}Os-^{187}Os systematics of Gorgona Island komatiites: implications for early growth of the inner core. *Earth Planet. Sci. Lett.* **206**, 411–426.

Brandon A. D., Norman M. D., Walker R. J. and Morgan J. W. (1999) ^{186}Os-^{187}Os systematics of Hawaiian picrites. *Earth Planet. Sci. Lett.* **174**, 25–42.

Brounce M. N., Stolper E. and Eiler J. (2017) Redox variations in Mauna Kea lavas, the oxygen fugacity of the Hawaiian plume, and the role of volcanic gases in Earth's oxygenation. *Proc. Natl. Acad. Sci.* **114**, 8997–9002.

Brounce M. N., Kelley K. A. and Cottrell E. (2014) Variations in $Fe^{+3}/\Sigma Fe$ of Mariana Arc basalts and mantle wedge fO_2. *J. Petrol.* **55**, 2513–2536.

Brügmann G., Arndt N., Hofmann A. and Tobschall H. (1987) Noble metal abundances in komatiite suites from Alexo, Ontario and Gorgona Island, Colombia. *Geochim. Cosmochim. Acta* **51**, 2159–2169.

Buffett B. A. (2003) The thermal state of Earth's core. *Science* **299**, 1675–1676.

Canil D. and Fedortchouk Y. (2001) Olivine-liquid partitioning of vanadium and other trace elements, with applications to modern and ancient picrites. *Can. Mineral.* **39**, 319–330.

Canil D. (1997) Vanadium partitioning and the oxidation state of Archaean komatiite magmas. *Nature* **389**, 842–845.

Canil D., O'Neill H., St C., Pearson D. G., Rudnick R., McDonough W. and Carswell D. (1994) Ferric iron in peridotites and mantle oxidation states. *Earth Planet. Sci. Lett.* **123**, 205–220.

Carmichael I. S. (1991) The redox states of basic and silicic magmas: a reflection of their source regions? *Contrib. Mineral. Petrol.* **106**, 129–141.

Catling D. C. (2014) The great oxidation event transition. *Treatise Geochem.* **6**, 177–195.

Catling D. C., Zahnle K. J. and McKay C. P. (2001) Biogenic methane, hydrogen escape, and the irreversible oxidation of early Earth. *Science* **293**, 839–843.

Chung S. L., Lee T. Y., Lo C. H., Wang P. L., Chen C. Y., Nguyen T. Y., Tran T. H. and Wu G. Y. (1997) Intraplate extention prior to continental extrusion along the Ailao Shan-Red River shear zone. *Geology* **25**, 311–314.

Chung S.-L., Jahn B.-M., Genyao W., Lo C.-H. and Bolin C. (1998) The Emeishan Flood Basalt in SW China: a mantle plume initiation model and its connection with continental breakup and mass extinction at the Permian-Triassic boundary. In Mantle Dynamics and Plate Tectonics in East Asia (eds. M. F. J. Flower, S.-L. Chung, C.-H. Lo and T.-Y. Lee). AGU Geodynamics Series 27, 47–58.

Ciborowski T. and Kerr A. C. (2016) Did mantle plume magmatism help trigger the Great Oxidation Event? *Lithos* **246–247**, 128–133.

Clarke D. B. and Upton B. G. J. (1971) Tertiary basalts of Baffin Island: field relations and tectonic setting. *Can. J. Earth Sci.* **8**, 248–258.

Cottrell E. and Kelley K. A. (2011) The oxidation state of Fe in MORB glasses and the oxygen fugacity of the upper mantle. *Earth Planet. Sci. Lett.* **305**, 270–282.

Cottrell E., Kelley K. A., Lanzirotti A. and Fischer R. A. (2009) High-precision determination of iron oxidation state in silicate glasses using XANES. *Chem. Geol.* **268**, 167–179.

Dale C., Pearson D. G., Starkey N., Stuart F., Ellam R., Larsen L., Fitton J. M. and Macpherson C. (2009) Osmium isotopes in Baffin Island and West Greenland picrites: implications for the $^{187}Os/^{188}Os$ composition of the convecting mantle and the nature of high $^{3}He/^{4}He$ mantle. *Earth Planet. Sci. Lett.* **278**, 267–277.

Dauphas N. (2009) Iron isotopes may reveal the redox conditions of mantle melting from Archean to Present. *Earth Planet. Sci. Lett.* **288**, 255–267.

Day J. M. D. (2016) Evidence against an ancient non-chondritic mantle source for North Atlantic Igneous Province lavas. *Chem. Geol.* **440**, 91–100.

Debaill V., O'Neill C., Brandon A. D., Haenecour P., Yin Q.-Z., Matielli N. and Treiman A. H. (2013) Stagnant-lid tectonics in early Earth revealed by ^{142}Nd variations in late Archean rocks. *Earth Planet. Sci. Lett.* **373**, 83–92.

Delano J. W. (2001) Redox history of the Earth's interior since ~3900 Ma: implications for prebiotic molecules. *Orig. Life Evol. Biosp.* **31**, 311–341.

De Leeuw G. D., Ellam R., Stuart F. and Carlson R. (2017) $^{142}Nd/^{144}Nd$ inferences on the nature and origin of the source of high $^{3}He/^{4}He$ magmas. *Earth Planet. Sci. Lett.* **472**, 62–68.

Deutsch E. R., Kristjansson L. G. and May B. T. (1971) Remanent magnetism of lower Tertiary lavas on Baffin Island. *Can. J. Earth Sci.* **8**, 1542–1552.

Dupre B. and Echeverria L. M. (1984) Pb isotopes of Gorgona island (Colombia): isotopic variations correlated with magma type. *Earth Planet. Sci. Lett.* **67**, 186–190.

Echeverria L. (1980) Tertiary or Mesozoic komatiites from Gorgona Island, Colombia: field relations and geochemistry. *Contrib. Mineral. Petrol.* **73**, 253–266.

Evans K. A. (2012) The redox budget of subduction zones. *Earth-Sci. Rev.* **113**, 11–32.

Ernst R. and Bleeker W. (2010) Large igneous provinces (LIPs), giant dyke swarms, and mantle plumes: significance for breakup events within Canada and adjacent regions from 2.5 Ga to the present. *Can. J. Earth Sci.* **47**, 695–739.

Farquhar J., Bao H. and Thiemens M. (2000) Atmospheric influence of Earth's earliest sulfur cycle. *Science* **289**, 756–758.

Fischer W. W., Hemp J. and Johnson J. E. (2016) Evolution of oxygenic photosynthesis. *Ann. Rev. Earth Planet. Sci.* **44**, 647–683.

Foley S. F. (2011) A reappraisal of redox melting in the Earth's mantle as a function of tectonic setting and time. *J. Petrol.* **52**, 1363–1391.

Francis D. (1985) The Baffin-Bay lavas and the value of picrites as analogs of primary magmas. *Contrib. Mineral. Petrol.* **89**, 144–154.

Frost D., Mann U., Asahara Y. and Rubie D. (2008) The redox state of the mantle during and just after core formation. *Phil. Trans. Roy. Soc. A: Math. Phys. Eng. Sci.* **366**, 4315–4337.

Frost D. J. and McCammon C. A. (2008) The redox state of Earth's mantle. *Ann. Rev. Earth Planet. Sci.* **36**, 389–420.

Gaillard F., Scaillet B. and Arndt N. T. (2011) Atmospheric oxygenation caused by a change in volcanic degassing pressure. *Nature* **478**, 229–233.

Ganne J. and Feng X. (2017) Primary magmas and mantle temperatures through time. *Geochem. Geophys. Geosyst.* **18**, 872–888.

Gansser A., Dietrich V. J. and Cameron W. E. (1979) Paleogene komatiites from Gorgona Island. *Nature* **278**, 545–546.

Gerlach T. M. (1993) Oxygen buffering of Kilauea volcanic gases and the oxygen fugacity of Kilauea basalt. *Geochim. Cosmochim. Acta* **57**, 795–814.

Gerya T. (2014) Precambrian geodynamics: concepts and models. *Gondwana Res.* **25**, 442–463.

Grocke S. B., Cottrell E., Silva S. D. and Kelley K. A. (2016) The role of crustal and eruptive processes versus source variations in controlling the oxidation state of iron in Central Andean magmas. *Earth Planet. Sci. Lett.* **440**, 92–104.

Gumsley A. P., Chamberlain K. R., Bleeker W., Söderlund U., de Kock M. O., Larsson E. R. and Bekker A. (2017) Timing and tempo of the Great Oxidation Event. *Proc. Natl. Acad. Sci.* **114**, 1811–1816.

Hanski E. and Huhma H. (2005) Central Lapland greenstone belt. In *Precambrian Geology of Finland – Key to the Evolution of the Fennoscandian Shield* (eds. M. Lehtinen, P. A. Nurmi and O. T. Rämö). Elsevier Science B.V, Amsterdam, pp. 139–193.

Hanski E., Walker R. J., Huhma H., Polyakov G. V., Balykin P. A., Hoa T. T. and Phuong N. T. (2004) Origin of the Permian-Triassic komatiites, northwestern Vietnam. *Contrib. Mineral. Petrol.* **147**, 453–469.

Hanski E., Huhma H., Rastas P. and Kamenetsky V. S. (2001) The Palaeoproterozoic komatiite-picrite association of Finnish Lapland. *J. Petrol.* **42**, 855–876.

Helz R. T. (2012) Trace Element Analyses of Core Samples from the 1967–1988 Drillings of Kilauea Iki Lava Lake, Hawaii. U.S. Geol. Surv., Open-file Report 2012–1050.

Hemond C., Arndt N. T., Lichtenstein U., Hofmann A. W., Askarsson N. and Steinthorsson S. (1993) The heterogeneous Iceland plume: Nd–Sr–O isotopes and trace element constraints. *J. Geophys. Res.* **98**, 15833–15850.

Herd C. D. (2008) Basalts as probes of planetary interior redox state. *Rev. Mineral. Geochem.* **68**, 527–553.

Herzberg C., Condie K. and Korenaga J. (2010) Thermal history of the Earth and its petrological expression. *Earth Planet. Sci. Lett.* **292**, 79–88.

Hibbert K. E. J., Williams H. M., Kerr A. C. and Puchtel I. S. (2012) Iron isotopes in ancient and modern komatiites: evidence in support of an oxidised mantle from Archean to present. *Earth Planet. Sci. Lett.* **321–322**, 198–207.

Holland H. D. (2002) Volcanic gases, black smokers, and the great oxidation event. *Geochim. Cosmochim. Acta* **66**, 3811–3826.

Huhma H., Hanski E., Kontinen A., Vuollo J., Mänttäri I. and Lahaye Y. (2018) Sm-Nd and U-Pb isotope geochemistry of the Paleoproterozoic mafic magmatism in eastern and northern Finland. Geol. Surv. Finl., Bull. 405.

Hulbert L., Stern R., Kyser T. K., Pearson J., Lesher M. and Grinenko L., (1994) The Winnipegosis komatiite belt, central Manitoba. Manitoba Mining and Minerals Convention 1994, Program and Abstracts, p. 21.

Humayun M., Qin L. and Norman M. D. (2004) Geochemical evidence for excess iron in the mantle Beneath Hawaii. *Science* **306**, 91–94.

Huppert H. E. and Sparks R. S. J. (1985) Komatiites I: Eruption and flow. *J. Petrol.* **26**, 694–725.

Huppert H. E., Sparks R. S. J., Turner J. S. and Arndt N. T. (1984) Emplacement and cooling of komatiite lavas. *Nature* **309**, 19–22.

Ireland T. J., Walker R. J. and Brandon A. D. (2011) ^{186}Os–^{187}Os systematics of Hawaiian picrites revisited: new insights into Os isotopic variations in ocean island basalts. *Geochim. Cosmochim. Acta* **75**, 4456–4475.

Jackson M. G., Carlson R. W., Kurz M. D., Kempton P. D., Francis D. and Blusztajn J. (2010) Evidence for the survival of the oldest terrestrial mantle reservoir. *Nature* **466**, 853–856.

Kasting J. F., Eggler D. H. and Raeburn S. P. (1993) Mantle redox evolution and the oxidation state of the Archean atmosphere. *J. Geol.* **101**, 245–257.

Kelley K. A. and Cottrell E. (2012) The influence of magmatic differentiation on the oxidation state of Fe in a basaltic arc magma. *Earth Planet. Sci. Lett.* **329–330**, 109–121.

Kent A. J. R., Stolper E. M., Francis D., Woodhead J., Frei R. and Eiler J. (2004) Mantle heterogeneity during the formation of the North Atlantic Igneous Province: constraints from trace element and Sr–Nd–Os–O isotope systematics of Baffin Island picrites. *Geochem. Geophys. Geosyst.* **5**, 2004GC000743.

Kerr A. C. (2005) La Isla de Gorgona, Colombia: a petrological enigma? *Lithos* **84**, 77–101.

Kerr A. C., Marriner G. F., Arndt N. T., Tarney J., Nivia A., Saunders A. D. and Duncan R. A. (1996) The petrogenesis of Gorgona komatiites, picrites and basalts: new field, petrographic and geochemical constraints. *Lithos* **37**, 245–260.

Kress V. C. and Carmichael I. S. E. (1991) The compressibility of silicate liquidus containing Fe_2O_3 and the effect of composition, temperature, oxygen fugacity and pressure on their redox states. *Contrib. Mineral. Petrol.* **103**, 82–92.

Krissansen-Totton J., Buick R. and Catling D. C. (2015) A statistical analysis of the carbon isotope record from the Archean to Phanerozoic and implications for the rise of oxygen. *Am. J. Sci.* **315**, 275–316.

Kump L. R. and Barley M. E. (2007) Increased subaerial volcanism and the rise of atmospheric oxygen 2.5 billion years ago. *Nature* **448**, 1033–1036.

Kurz M. D., Meyer P. S. and Sigurdsson H. (1985) Helium isotopic systematics within the neovolcanic zones of Iceland. *Earth Planet. Sci. Lett.* **74**, 291–305.

Labrosse S., Poirier J.-P. and Le Mouël J.-L. (2001) The age of the inner core. *Earth Planet. Sci. Lett.* **190**, 111–123.

Larsen L. M. and Pedersen A. K. (2000) Processes in high-Mg, high T Magmas: Evidence from olivine, chromite and glass in paleogene picrites from West Greenland. *J. Petrol.* **41**(7), 1071–1098.

Laubier M., Grove T. L. and Langmuir C. H. (2014) Trace element mineral/melt partitioning for basaltic and basaltic andesitic melts: an experimental and laser ICP-MS study with application to the oxidation state of mantle source regions. *Earth Planet. Sci. Lett.* **392**, 265–278.

Lécuyer C. and Ricard Y. (1999) Long-term fluxes and budget of ferric iron: implication for the redox states of the Earth's mantle and atmosphere. *Earth Planet. Sci. Lett.* **165**, 197–211.

Lecuyer C., Gruau G., Anhaeusser C. R. and Fourcade S. (1994) The origin of fluids and the effect of metamorphism on the primary chemical compositions of Barberton komatiites: new evidence from geochemical (REE) and isotopic (Nd, O, H, $^{39}Ar/^{40}Ar$) data. *Geochim. Cosmochim. Acta* **58**, 969–984.

Lee C.-T. A., Yeung L. Y., McKenzie N. R., Yokoyama Y., Ozaki K. and Lenardic A. (2016) Two-step rise of atmospheric oxygen linked to the growth of continents. *Nat. Geosci.* **9**, 417–424.

Lee C.-T. A., Leeman W. P., Canil D. and Li Z.-X. A. (2005) Similar V/Sc Systematics in MORB and Arc Basalts: implications for the oxygen fugacities of their mantle source regions. *J. Petrol.* **46**(11), 2313–2336.

Le Voyer M., Cottrell E., Kelley K. A., Brounce M. and Hauri E. H. (2015) The effect of primary versus secondary processes on the volatile content of MORB glasses: an example from the equatorial Mid-Atlantic Ridge (5°N-3°S). *J. Geophys. Res.* **120**, 125–144.

Li Z. X. A. and Lee C. T. A. (2004) The constancy of upper mantle fO_2 through time inferred from V/Sc ratios in basalts. *Earth Planet. Sci. Lett.* **228**, 483–493.

Lo C.-H., Chung S.-L., Lee T.-Y. and Wu G. (2002) Age of the Emeishan flood magmatism and relations to Permian-Triassic boundary events. *Earth Planet. Sci. Lett.* **198**, 449–458.

Ludwig K. R. (2003) ISOPLOT 3.00. A Geochronological Toolkit for Microsoft Excel. Berkeley Geochronol. Cent. Spec. Publ. 4.

Luguet A., Pearson D. G., Nowell G. M., Dreher S. T., Coggon J. A., Spetsius Z. V. and Parman S. W. (2008) Enriched Pt-Re-Os isotope systematics in plume lavas explained by metasomatic sulfides. *Science* **319**, 453–456.

Lyons T. W., Reinhard C. T. and Planavsky N. J. (2014) The rise of oxygen in Earth's early ocean and atmosphere. *Nature* **506**, 307–315.

Mallmann G. and O'Neill H. St. C. (2013) Calibration of an empirical thermometer and oxybarometer based on the partitioning of Sc, Y and V between olivine and silicate melt. *J. Petrol.* **54**, 933–949.

Mallmann G. and O'Neill H. St. C. (2009) The crystal/melt partitioning of V during mantle melting as a function of oxygen fugacity compared with some other elements (Al, P, Ca, Sc, Ti, Cr, Fe, Ga, Y, Zr and Nb). *J. Petrol.* **50**, 1765–1794.

Mathez E. A. (1976) Sulfur solubility and magmatic sulfides in submarine basalt glass. *J. Geophys. Res.* **81**, 4269–4276.

Matsui T. and Abe Y. (1986) Formation of a 'magma ocean' on the terrestrial planets due to the blanketing effect of an impact-induced atmosphere. *Earth Moon Planets.* **34**, 223–230.

McGregor C. R. (2011) Open File OF2011–1: GIS Compilation of Relogged Sub-Phanerozoic Precambrian Exploration Drillcore from the Thompson Nickel Belt, Eastern Flin Flon Belt and Winnipegosis Komatiite Belt (Parts of NTS 63B, C, F, G, J, K).

Mertzman S. A. (2000) K-Ar results from the southern Oregon - northern California Cascade range. *Oregon Geol.* **62**, 99–122.

Métrich N., Berry A. J., O'Neill H., St C. and Susini J. (2009) The oxidation state of sulfur in synthetic and natural glasses

determined by X-ray absorption spectroscopy. *Geochim. Cosmochim. Acta* **73**, 2382–2399.

Moore W. B. and Webb A. A. (2013) Heat-pipe Earth. *Nature* **501**, 501–505.

Moussallam Y., Edmonds M., Scaillet B., Peters N., Gennaro E., Sides I. and Oppenheimer C. (2016) The impact of degassing on the oxidation state of basaltic magmas: a case study of Kīlauea volcano. *Earth Planet. Sci. Lett.* **450**, 317–325.

Moussallam Y., Oppenheimer C., Scaillet B., Gaillard F., Kyle P., Peters N., Hartley M., Berlo K. and Donovan A. (2014) Tracking the changing oxidation state of Erebus magmas, from mantle to surface, driven by magma ascent and degassing. *Earth Planet. Sci. Lett.* **393**, 200–209.

Mundl A., Touboul M., Jackson M. G., Day J. M., Kurz M. D., Lekic V., Helz R. and Walker R. J. (2017) Tungsten-182 heterogeneity in modern ocean island basalts. *Science* **356**, 66–69.

Mutanen T. and Huhma H. (2001) U-Pb geochronology of the Koitelainen, Akanvaara and Keivitsa layered intrusions and related rocks. In Radiometric Age Determinations from Finnish Lapland and Their Bearing on the Timing of Precambrian Volcano-Sedimentary Sequences (ed. M. Vaasjoki). Geol. Surv. Finl., Spec. Pap. 33, 229–246.

Nesbitt R. W. and Sun S.-S. (1976) Geochemistry of Archean spinifex-textured peridotites and magnesian and low-magnesian tholeiites. *Earth Planet. Sci. Lett.* **31**, 433–453.

Nicklas R. W. and Puchtel I.S. (2016) Preservation of magma ocean redox heterogeneities: evidence from Paleoarchean komatiites. Abstract V11D-03, presented at 2016 Fall Meeting, AGU, San Francisco, California, 12–16 Dec, 2016.

Nicklas R. W., Puchtel I. S. and Ash R. D. (2016) High-precision determination of the oxidation state of komatiite lavas using vanadium liquid-mineral partitioning. *Chem. Geol.* **433**, 36–45.

Nicklas R. W., Puchtel I. S. and Ash R. D. (2018) Redox state of the Archean mantle: evidence from V partitioning in 3.5–2.4 Ga komatiites. *Geochim. Cosmochim. Acta* **222**, 447–466.

Nisbet E. G., Cheadle M. J., Arndt N. T. and Bickle M. J. (1993) Constraining the potential temperature of the Archaean mantle: a review of the evidence from komatiites. *Lithos* **30**, 291–307.

Norman M. D. and Garcia M. O. (1999) Primitive magmas and source characteristics of the Hawaiian plume: petrology and geochemistry of shield picrites. *Earth Planet. Sci. Lett.* **168**, 27–44.

Ono S. (2017) Photochemistry of sulfur dioxide and the origin of mass-independent isotope fractionation in Earth's atmosphere. *Ann. Rev. Earth Planet. Sci.* **45**, 301–329.

Padron-Navarta J. A., Sanchez-Vizcaino V. L., Garrido C. J. and Gomez-Pugnaire M. T. (2011) Metamorphic record of high-pressure dehydration of antigorite serpentinite to chlorite harzburgite in a subduction setting (Cerro del Almirez, Nevado-Filabride Complex, Southern Spain). *J. Petrol.* **52**, 2047–2078.

Parkinson I. J. and Arculus R. J. (1999) The redox state of subduction zones: insights from arc-peridotites. *Chem. Geol.* **160**, 409–423.

Pedersen A. K., Larsen L. M., Riisager P. and Dueholm K. S. (2002) Rates of volcanic deposition, facies changes and movements in a dynamic basin: the Nuussuaq Basin, West Greenland, around the C27n–C26r transition. In The North Atlantic Igneous Province: Stratigraphy, Tectonics, Volcanic and Magmatic Processes (eds. D. W. Jolley and B. R. Bell). Geol. Soc. London, Spec. Publ. 197, 157–181.

Pitcher L., Helz R. T., Walker R. J. and Piccoli P. M. (2009) Fractionation of the platinum-group elements and Re during crystallization of basalt in Kilauea Iki Lava Lake, Hawaii. *Chem. Geol.* **260**, 196–210.

Planavsky N. J., Asael D., Hofmann A., Reinhard C. T., Lalonde S. V., Knudsen A., Wang X., Ossa Ossa F., Pecoits E., Smith A. J. B., Beukes N. J., Bekker A., Johnson T. M., Konhauser K. O., Lyons T. W. and Rouxel O. J. (2014) Evidence for oxygenic photosynthesis half a billion years before the Great Oxidation Event. *Nat. Geosci.* **7**, 283.

Polyakov G. V., Balykin P. A., Glotov A. I., Tran Q. H., Ngo T. P., Hoang H. T. and Bui A. N. (1991) Permian-Triassic association of high-magnesian volcanic rocks of the Song Da zone (north-western Vietnam). *Sov. Geol. Geophys.* **32**, 1–11.

Puchtel I. S., Blichert-Toft J., Touboul M., Horan M. F. and Walker R. J. (2016a) The coupled ^{182}W–^{142}Nd record of early terrestrial mantle differentiation. *Geochem. Geophys. Geosys.* **17**, 2168–2193.

Puchtel I. S., Touboul M., Blichert-Toft J., Walker R. J., Brandon A. D., Nicklas R. W., Kulikov V. S. and Samsonov A. V. (2016b) Lithophile and siderophile element systematics of the Earth's mantle at the Archean-Proterozoic boundary: evidence from 2.4 Ga komatiites. *Geochim. Cosmochim. Acta* **180**, 227–255.

Puchtel I. S., Walker R. J., Touboul M., Nisbet E. G. and Byerly G. R. (2014) Insights into early Earth from the Pt-Re-Os isotope and highly siderophile element systematics of Baberton komatiites. *Geochim. Cosmochim. Acta* **125**, 394–413.

Puchtel I. S., Blichert-Toft J., Touboul M., Walker R. J., Byerly G., Nisbet E. G. and Anhaeusser C. R. (2013) Insights into early Earth from Barberton komatiites: evidence from lithophile isotope and trace element systematics. *Geochim. Cosmochim. Acta* **108**, 63–90.

Puchtel I. S., Walker R. J., Anhaeusser C. R. and Gruau G. (2009) Re-Os isotope systematics and HSE abundances of the 3.5 Ga Schapenburg komatiites, South Africa: hydrous melting or prolonged survival of primordial heterogeneities in the mantle? *Chem. Geol.* **262**, 355–369.

Puchtel I. S., Brandon A. D., Humayun M. and Walker R. J. (2005) Evidence for the early differentiation of the core from Pt-Re-Os isotope systematics of 2.8-Ga komatiites. *Earth Planet. Sci. Lett.* **237**, 118–134.

Puchtel I. S., Humayun M., Campbell A., Sproule R. and Lesher C. M. (2004) Platinum group element geochemistry of komatiites from the Alexo and Pyke Hill areas, Ontario, Canada. *Geochim. Cosmochim. Acta* **68**, 1361–1383.

Puchtel I. S., Arndt N. T., Hofmann A. W., Haase K. M., Kröner A., Kulikov V. S., Kulikova V. V., Garbe-Schonberg C. D. and Nemchin A. A. (1998a) Petrology of mafic lavas within the Onega plateau, central Karelia: evidence for 2.0 Ga plume-related continental crustal growth in the Baltic Shield. *Contrib. Mineral. Petrol.* **130**, 134–153.

Puchtel I., Brügmann G. and Hofmann A. (1998b) Precise Re–Os mineral isochron and Pb–Nd–Os isotope systematics of a mafic–ultramafic sill in the 2.0 Ga Onega plateau (Baltic Shield). *Earth Planet. Sci. Lett.* **170**, 447–461.

Revillon S., Chauvel C., Arndt N. T., Pik R., Martineau F., Fourcade S. and Marty B. (2002) Heterogeneity of the Caribbean plateau mantle source: heterogeneity of the Caribbean plateau mantle source: Sr, O and He isotopic compositions of olivine and clinopyroxene from Gorgona island. *Earth Planet. Sci. Lett.* **205**, 91–106.

Revillon S., Arndt N. T., Chauvel C. and Hallot E. (2000) Geochemical study of ultramafic volcanic and plutonic rocks from Gorgona island, Colombia: the plumbing system of an oceanic plateau. *J. Petrol.* **41**, 1127–1153.

Richter D. H. and Moore J. G. (1966) Petrology of the Kilauea Iki Lava Lake, Hawaii, U.S. Geol. Surv. Prof. Pap. 537-B.

Rizo H., Walker R. J., Carlson R. W., Horan M. F., Mukhopadhyay S., Manthos V., Francis D. and Jackson M. G. (2016)

Preservation of Earth-forming events in the tungsten isotopic composition of modern flood basalts. *Science* **352**, 809–812.
Robillard I., Francis D. and Ludden J. N. (1992) The relationship between E- and N-type magmas in the Baffin Bay lavas. *Contrib. Mineral. Petrol.* **112**, 230–241.
Roeder P. L. and Emslie R. F. (1970) Olivine-liquid equilibrium. *Contrib. Mineral. Petrol.* **29**, 275–282.
Sack R. O., Carmichael I. S. E., Rivers M. and Ghiorso M. S. (1980) Ferric-ferrous equilibria in natural silicate liquids at 1 bar. *Contrib. Mineral. Petrol.* **75**, 369–376.
Schidlowski M. (1988) A 3,800-million-year isotopic record of life from carbon in sedimentary rocks. *Nature* **333**, 313–318.
Serrano L., Ferrari L., Martinez M. L., Petrone C. M. and Jaramillo C. (2011) An integrative geologic, geochronologic and geochemical study of Gorgona Island, Colombia: implications for the formation of the Caribbean Large Igneous Province. *Earth Planet. Sci. Lett.* **309**, 324–336.
Shu Q., Brey G. P., Hoefer H. E., Zhao Z. and Pearson D. G. (2016) Kyanite/corundum eclogites from the Kaapvaal Craton: subducted troctolites and layered gabbros from the Mid- to Early Archean. *Contrib. Mineral. Petrol.* **171**, 11. https://doi.org/10.1007/s00410-015-1225-5.
Sinton C. W., Duncan R. A., Storey M., Lewis J. and Estrada J. J. (1998) An oceanic flood basalt province within the Caribbean plate. *Earth Planet. Sci. Lett.* **155**, 221–235.
Sizova E., Gerya T., Brown M. and Perchuk L. (2010) Subduction styles in the Precambrian: insight from numerical experiments. *Lithos* **116**, 209–229.
Sossi P. A., Eggins S. M., Nesbitt R. W., Nebel O., Hergt J. M., Campbell I. H., O'Neill H., St C., Van Kranendonk M. and Davies D. R. (2016) Petrogenesis and geochemistry of Archean komatiites. *J. Petrol.* **57**, 147–184.
Sossi P. A., Foden J. D. and Halverson G. P. (2012) Redox-controlled iron isotope fractionation during magmatic differentiation: an example from the Red Hill intrusion, S. Tasmania. *Contrib. Mineral. Petrol.* **164**, 757–772.
Starkey N., Stuart F. M., Ellam R. M., Fitton J. G., Basu S. and Larsen L. M. (2009) Helium isotopes in early Iceland plume picrites: constraints on the composition of high $^{3}He/^{4}He$ mantle. *Earth Planet. Sci. Lett.* **277**, 91–100.
Stolper D. A. and Keller C. B. (2018) A record of deep-ocean dissolved O_2 from the oxidation state of iron in submarine basalts. *Nature* **553**, 323–327.
Stuart F. M., Lass-Evans S., Fitton J. G. and Ellam R. M. (2003) High $^{3}He/^{4}He$ ratios in picritic basalts from Baffin Island and the role of a mixed reservoir in mantle plumes. *Nature* **424**, 57–59.
Thompson P. M. E., Kempton P. D., White R. V., Kerr A. C., Tarney J., Saunders A. D., Fitton J. G. and McBirney A. (2003) Hf–Nd isotope constraints on the origin of the Cretaceous Caribbean plateau and its relationship to the Galapagos plume. *Earth Planet. Sci. Lett.* **217**(1–2), 59–75.
Tonks W. B. and Melosh H. J. (1993) Magma ocean formation due to giant impacts. *J. Geophys. Res.* **98**(E3), 5319–5333.
Touboul M., Puchtel I. S. and Walker R. J. (2012) ^{182}W evidence for long-term preservation of early mantle differentiation products. *Science* **335**, 1065–1069.
Trail D., Watson E. B. and Tailby N. D. (2011) The oxidation state of Hadean magmas and implications for early Earth's atmosphere. *Nature* **480**, 79–82.
Viljoen M. J. and Viljoen R. P. (1969) The geology and geochemistry of the Lower Ultramafic Unit of the Onverwacht Group and a proposed new class of igneous rocks. Geol. Soc. S. Afr., Spec. Publ. 2, 55–86.
Walker R. J., Storey M., Kerr A. C., Tarney J. and Arndt N. T. (1999) Implications of ^{187}Os isotopic heterogeneities in a mantle plume: evidence from Gorgona Island and Curaçao. *Geochim. Cosmochim. Acta* **63**, 713–728.
Wang C. Y., Zhou M.-F. and Qi L. (2007) Permian flood basalts and mafic intrusions in the Jinping (SW China)-Song Da (northern Vietnam) district: mantle sources, crustal contamination and sulfide segregation. *Chem. Geol.* **243**, 317–343.
Waterton P., Pearson D. G., Kjarsgaard B., Hulbert L., Locock A., Parman S. and Davis B. (2017) Age, origin and thermal evolution of ultra-fresh ~1.9 Ga Winnipegosis komatiites, Manitoba, Canada. *Lithos* **268–271**, 114–130.
White R. and McKenzie D. (1989) Magmatism at rift zones: the generation of volcanic continental margins and flood basalts. *J. Geophys. Res.* **94**, 7685–7729.
Willbold M., Mojzsis S. J., Chen H. W. and Elliott T. (2015) Tungsten isotope composition of the Acasta Gneiss Complex. *Earth Planet. Sci. Lett.* **419**, 168–177.
Williams H. M., Nielsen S. G., Renac C., Griffin W. L., O'Reilly S. Y., McCammon C. A., Pearson N., Viljoen F., Alt J. C. and Halliday A. N. (2009) Fractionation of oxygen and iron isotopes by partial melting processes: implications for the interpretation of stable isotope signatures in mafic rocks. *Earth Planet. Sci. Lett.* **283**, 156–166.
Williams H. M., Peslier A. H., McCammon C., Halliday A. N., Levasseur S., Teutsch N. and Burg J. P. (2005) Systematic iron isotope variations in mantle rocks and minerals: the effects of partial melting and oxygen fugacity. *Earth Planet. Sci. Lett.* **235**, 435–452.
Wood D. H. (1991) Oxygen barometry of spinel peridotites. *Rev. Mineral. Geochem.* **25**, 417–432.
Wood B. J., Walter M. J. and Wade J. (2006) Accretion of the Earth and segregation of its core. *Nature* **441**, 825–833.
Woodland A. and Koch M. (2003) Variation in oxygen fugacity with depth in the upper mantle beneath the Kaapvaal craton, Southern Africa. *Earth Planet. Sci. Lett.* **214**, 295–310.
Wright T. L. (1973) Magma mixing as illustrated by the 1959 eruption. Kilauea Volcano, Hawaii. *Geol. Soc. Am. Bull.* **84**, 849–858.
Zahnle K. J., Catling D. C. and Claire M. W. (2013) The rise of oxygen and the hydrogen hourglass. *Chem. Geol.* **362**, 26–34.

Associate editor: Munir Humayun